



## Original Article

# Experimental studies and thermodynamic assessment of the Ba-Mo-O system by the CALPHAD method



A.L. Smith<sup>a,\*</sup>, M. Rutten<sup>a</sup>, L. Herrmann<sup>a</sup>, E. Epifano<sup>a</sup>, R.J.M. Konings<sup>b</sup>, E. Colineau<sup>b</sup>, J.-C. Griveau<sup>b</sup>, C. Guéneau<sup>c</sup>, N. Dupin<sup>d</sup>

<sup>a</sup> Delft University of Technology, Faculty of Applied Sciences, Radiation Science & Technology Department, Mekelweg 15, 2629 JB Delft, The Netherlands

<sup>b</sup> European Commission, Joint Research Centre (JRC), Karlsruhe, Germany

<sup>c</sup> Université Paris-Saclay, CEA, Service de la Corrosion et du Comportement des Matériaux dans leur Environnement, 91191 Gif-sur-Yvette, France

<sup>d</sup> Calcul Thermodynamique, 3 rue de l'avenir, 63670 Orcet, France

## ARTICLE INFO

### Keywords:

Barium-molybdenum-oxygen system  
Differential Scanning Calorimetry  
Thermal-relaxation calorimetry  
XANES  
CALPHAD

## ABSTRACT

Thermodynamic measurements on BaMoO<sub>4</sub>, BaMoO<sub>3</sub> and BaMo<sub>3</sub>O<sub>10</sub> are reported, that served as input for the development of a thermodynamic model of the Ba-Mo-O system using the CALPHAD methodology. The valence states of molybdenum in BaMoO<sub>4</sub> and BaMoO<sub>3</sub> were confirmed to be VI and IV, respectively, from X-ray Absorption Near Edge Structure Spectroscopy measurements at the Mo K-edge. The heat capacity at low temperatures of these compounds was obtained from thermal-relaxation calorimetry. Phase equilibrium data in the BaMoO<sub>4</sub>-MoO<sub>3</sub> section were also measured, and the transition enthalpy associated with the peritectic decomposition of BaMo<sub>3</sub>O<sub>10</sub> was determined using Differential Scanning Calorimetry. The developed thermodynamic model used the compound energy formalism for intermediate compounds, and an ionic two-sublattice model for the liquid phase. The optimized Gibbs energies were assessed with respect to the known thermodynamic and phase equilibrium data. A good agreement is generally obtained, but a number of ill-defined data were also identified.

## 1. Introduction

The chemistry of fission product (FP) elements in irradiated nuclear fuel, and more particularly of volatile and semi-volatile elements, is of paramount importance, as FPs are the main source for the radiological consequences of a severe accident (SA) with release to the environment. Barium and molybdenum are generated with a high fission yield (~11% and ~25%, respectively [1]) during irradiation of the UO<sub>2</sub> or (U,Pu)O<sub>2</sub> ceramic fuel used in Light Water Reactors (LWRs), and represent key elements for the evaluation of the source term. They are classified as semi-volatile fission products, which implies that their release kinetics are dependent on the redox conditions of the surrounding environment, and are determined by the evaporation of the chemical compounds formed in the irradiated fuel [1]. The association of barium with molybdenum in the nuclear fuel in the form of oxide precipitates at grain boundaries was recently confirmed from the FPT2 test of the PHEBUS Fission Product Program [2]. However, the exact chemical form of barium and molybdenum in the fuel is rather complex, and changes with time in relation with the burnup, temperature and oxygen potential

conditions. The severe accident at the Fukushima-Daiichi Nuclear Power Station (FDNPS) has initiated a renewed interest in the behaviour of radionuclides with a potential long-term radiological impact such as those of Ba, Sr, U, Pu, and minor actinides. To respond to this necessity, the TCOFF project (Thermodynamic Characterization of Fuel Debris and Fission Products Based on Scenario Analysis of Severe Accident Progression at Fukushima-Daiichi Nuclear Power Station) was launched in 2017 under the auspices of the OECD/NEA [3], and the experimental study of the Ba-Mo-O system as outlined in this work constitutes a contribution to that initiative.

The solubility of barium in the (U,Pu)O<sub>2</sub> fuel matrix is very low due to its large ionic radius. At low oxygen potentials, it is found in the so-called grey phase of general formula (Ba,Sr,Cs)(Zr,U,Mo,RE)O<sub>3</sub> (RE = rare earths) with perovskite structure [4–8], while it is stable in the Ba(Mo,U)O<sub>4</sub> scheelite phase at high oxygen potentials [5,7–9]. For a thorough safety assessment of nuclear fuel behaviour under operation and in accidental conditions, a complete thermodynamic description of the multi-component system Ba-Sr-Cs-Zr-U-Pu-Mo-RE-O is therefore necessary. A number of thermodynamic and thermophysical data on the

\* Corresponding author.

E-mail address: [a.l.smith@tudelft.nl](mailto:a.l.smith@tudelft.nl) (A.L. Smith).

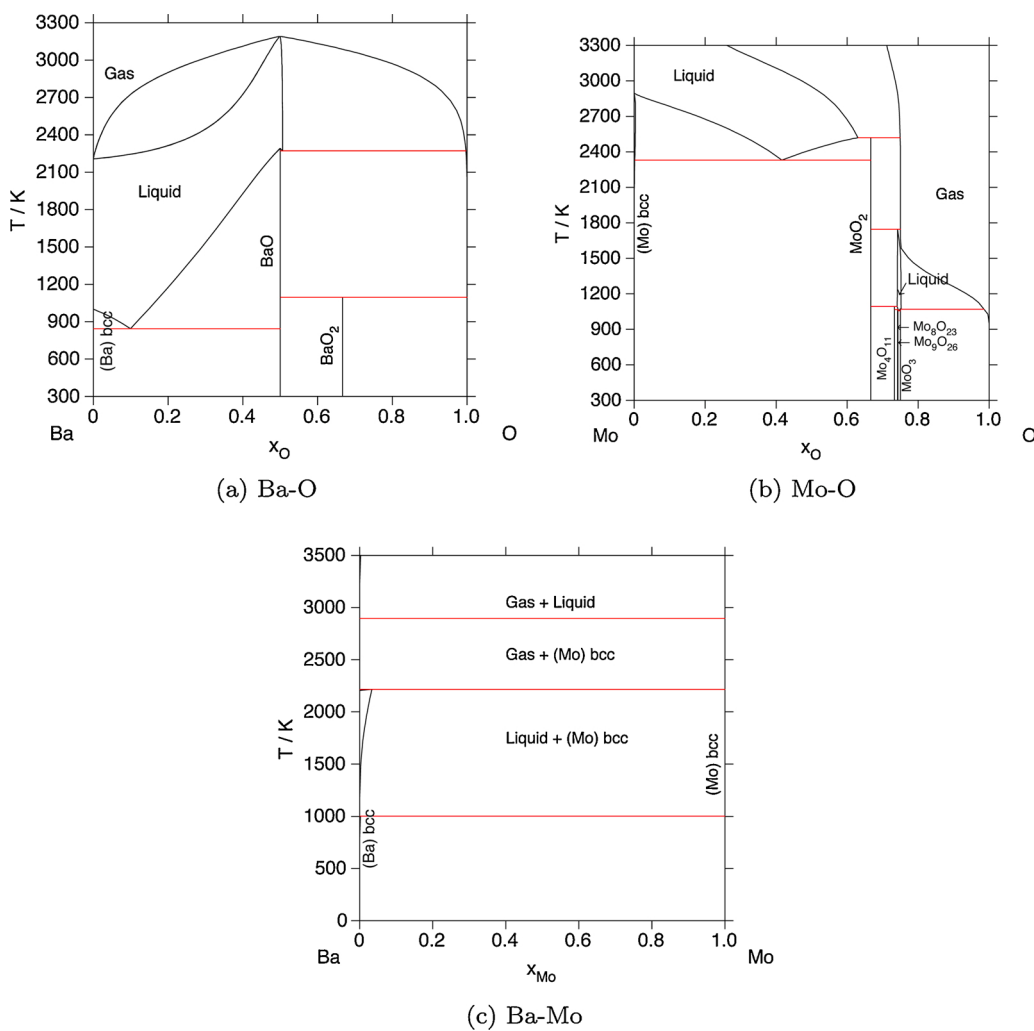


**Fig. 1.** Calculated binary phase diagrams of the (a) Ba-O (b) Mo-O and (c) Ba-Mo sub-systems using the TAF-ID models [10].

oxide phases formed in this system have been reported, but the knowledge is still limited. Nevertheless, a thermodynamic model has been developed using a CALPHAD (CALculation of PHase Diagram) approach within the TAF-ID project (Thermodynamics of Advanced Fuels – International Database) of the OECD/NEA [10]. More specifically, thermodynamic assessments of the Ba-Zr-O, Ba-U-O, Cs-Mo-O, Cs-U-O, Cs-Zr-O and Sr-Zr-O sub-systems have been made. The present work reports, next to the experimental studies, a CALPHAD model for the Ba-Mo-O system. It constitutes another building unit of the multi-element database of the TAF-ID. It also contributes to improving our knowledge of the still poorly understood thermochemistry of Ba and Mo fission product phases under severe accident conditions, which is key for a more reliable assessment of the source term in the SA codes.

The interest in the phase relationships in the Ba-Mo-O system does not limit itself to nuclear energy applications, however. Molybdate materials have received quite some attention in recent years because of their interesting properties for applications in photoluminescence [11–13], solid-state lasers [14,15], photocatalysts [16,17], gas sensing [18], microwave [19,20], or thermoelectric applications [21].  $\text{BaMoO}_4$  for instance shows photoluminescence [12,22] and can be used as host material for lanthanide cations (activated phosphors) [22].

In this work, we report a literature review of the thermodynamic and phase diagram data available on the Ba-Mo-O system, the synthesis and structural characterization of  $\text{BaMoO}_4$ ,  $\text{BaMoO}_3$ , and  $\text{BaMo}_3\text{O}_{10}$ , the measurement of the low-temperature heat capacity of the former two phases, the determination of the transition enthalpy associated with the

peritectic decomposition of  $\text{BaMo}_3\text{O}_{10}$ , and phase diagram measurements in the  $\text{BaMoO}_4$ - $\text{MoO}_3$  pseudo-binary section. Using these data as input, a CALPHAD model of the Ba-Mo-O system is then developed, that is compatible with the current descriptions and formalisms used in the TAF-ID database [10].

## 2. Review of literature data on the Ba-Mo-O system

### 2.1. Constituting binary sub-systems

A thermodynamic assessment of the three binary sub-systems, i.e. Ba-O, Ba-Mo, and Mo-O, is already available as part of the TAF-ID database of the OECD/NEA [10]. The latter were used as basis for the present assessment, and this work therefore focuses on the phase equilibria in the ternary system. The corresponding binary phase diagrams are shown in Fig. 1a–c.

#### 2.1.1. Binary Ba-Mo system

Ba and Mo are stable under the same crystalline phase, i.e. the bcc phase. However, their chemical and physical properties strongly differ, leading to a very small reciprocal solubility. The thermodynamic assessment of the Ba-Mo system was made in the framework of the Fuelbase project (2011) [23]. The corresponding parameters are listed in Tables C.1 and C.2. Due to the scarcity of data on this system, identical interaction parameters of the elements have been assumed in the liquid phase and in the bcc phase. This choice, made in the absence of

**Table 1**

Structural data on the Ba-Mo-O system. The phases for which no atomic positions have been reported are indicated with an \*.

Phase	Ox. state	Symmetry	Space group	Lattice parameters	Ref.
BaMoO <sub>4</sub>	+6	Tetragonal	<i>I</i> 4 <sub>1</sub> / <i>a</i> (88)	<i>a</i> = 0.5571(3) nm <i>c</i> = 1.2783(10) nm	[31]
Ba <sub>2</sub> MoO <sub>5</sub> *	+6	Orthorhombic	<i>Pnma</i> (62)	<i>a</i> = 0.7412 nm <i>b</i> = 0.5769 nm <i>c</i> = 1.1380 nm	[32]
Ba <sub>3</sub> MoO <sub>6</sub>	+6	Cubic	Fm $\bar{3}m$ (225)	<i>a</i> = 0.8600 nm	[33]
BaMo <sub>3</sub> O <sub>10</sub>	+6	Monoclinic	<i>P2</i> <sub>1</sub> (4)	<i>a</i> = 1.4695(2) nm <i>b</i> = 0.75704(7) nm <i>c</i> = 0.69618(6) nm $\beta$ = 100.381(8) $^\circ$	[34]
BaMo <sub>2</sub> O <sub>7</sub> *	+6	Unknown			[ref]
Ba <sub>2</sub> Mo <sub>5</sub> O <sub>17</sub> *	+6	Unknown			
Ba <sub>3</sub> Mo <sub>7</sub> O <sub>24</sub> *	+6	Unknown			
BaMoO <sub>3</sub>	+4	Cubic	Pm $\bar{3}m$ (221)	<i>a</i> = 0.404077(5) nm	[35]
Ba <sub>8</sub> / <sub>7</sub> Mo <sub>8</sub> O <sub>16</sub>	+3.71	Orthorhombic	<i>I</i> 4 (79)	<i>a</i> = 1.02160(5) nm <i>b</i> = 1.02160(5) nm <i>c</i> = 2.02449(8) nm	[36]
BaMo <sub>6</sub> O <sub>10</sub>	+3	Orthorhombic	<i>Pnma</i> (62)	<i>a</i> = 1.0154 nm <i>b</i> = 0.8641 nm <i>c</i> = 0.9184 nm	[37]
Ba <sub>3</sub> Mo <sub>18</sub> O <sub>28</sub>	+2.78	Monoclinic	<i>P2</i> <sub>1</sub> / <i>a</i> (14)	<i>a</i> = 0.9939(2) nm <i>b</i> = 0.9377(2) nm <i>c</i> = 1.3057(2) nm $\beta$ = 100.92(1) $^\circ$	[38]
Ba <sub>5</sub> (Mo <sub>4</sub> O <sub>6</sub> ) <sub>8</sub>	+2.69	Orthorhombic	<i>Pbam</i> (55)	<i>a</i> = 0.9517(1) nm <i>b</i> = 0.9822(1) nm <i>c</i> = 2.2813(4) nm	[39]

sufficient information, presumes similar first nearest neighbour coordination spheres in the liquid and *bcc* phases. The values of those interaction parameters have been derived in order to agree with the maximum solubility in the Ba liquid phase proposed by Massalski [24]. The formalisms used are described in Section 4.

### 2.1.2. Binary Ba-O system

The description initially present in the TAF-ID database for Ba-O was inherited from the Fuelbase project [23], based on the work by Zimmermann et al. [25]. The current description was built starting from the later assessment by Zhou et al. [26], that allows to better describe the heat capacity data for BaO<sub>2</sub>, following measurements reported subsequently to the work of Zimmermann et al. The description of the condensed phases BaO and BaO<sub>2</sub> by Zhou et al. have been modified to be consistent with the current models in the TAF-ID, however. The O<sub>2</sub><sup>2-</sup> species has not been considered in the model for the liquid phase, but rather has been replaced by a neutral O species. The stability of the liquid phase for compositions richer in oxygen than BaO has not been forced as in the original description, since no experimental information was available on this issue. The solid phases have been considered as stoichiometric. The BaO<sub>2</sub> homogeneity range modelled by Zimmermann et al. and by Zhou et al. is in fact considered too large according to [27] and [28]. This simplification implied a slight modification of the BaO<sub>2</sub> stoichiometric compound description, so as to maintain the agreement with the oxygen pressure data over the BaO-BaO<sub>2</sub> region. The description of the gaseous species in this system, and in particular of the binary species BaO and Ba<sub>2</sub>O, has been extracted from the substance SGTE (Scientific Group Thermochemical Europe) database. The thermodynamic function for the gaseous Ba<sub>2</sub>O<sub>2</sub> species was taken from the work of Zimmermann et al.

The optimized parameters are listed in Tables B.1 and B.2, and a comparison with the experimental data is shown in the Appendix (Fig. 17B.1), (Fig. 18B.2), (Fig. 19B.3), (Fig. 20B.4), (Fig. 21B.5), (Fig. 22B.6). The formalisms used for the different phases are described

**Table 2**

Experimental measurements of the enthalpy of formation of BaMoO<sub>4</sub>(cr).

Reference	Method	$\Delta_f H_m^{\circ}$ (298.15 K) (kJ · mol <sup>-1</sup> )
Tamman and Westerhold [40, 42]	Indirect (Reaction BaO + MoO <sub>3</sub> = BaMoO <sub>4</sub> at 560 K)	-(1540 ± 13)
Lavrent'ev et al. [41, 42]	Indirect (Oxygen potential of phase mixture of BaO, Mo, BaMoO <sub>4</sub> )	-(1586.8 ± 10.3)
Rezukhina [43, 47]	Indirect (EMF measurements)	-(1501.4 ± 10.7)
O'Hare [44]	Direct (solution calorimetry)	-(1545.6 ± 1.9)
Shukla et al. [45]	Direct (solution calorimetry)	-(1547.8 ± 3.6)
Singh et al. [46]	Indirect (EMF measurements) – second law	-(1557.5 ± 3.6)
	Indirect (EMF measurements) – third law	-(1536.8 ± 5.2)
Cordfunke and Konings [42]	Review	-(1544.0 ± 5.0)

in Section 4.

### 2.1.3. Binary Mo-O system

The Mo-O system is quite complex with five binary oxide compounds reported, i.e. MoO<sub>2</sub>, MoO<sub>3</sub>, Mo<sub>4</sub>O<sub>11</sub>, Mo<sub>8</sub>O<sub>23</sub>, Mo<sub>9</sub>O<sub>26</sub>, also treated as stoichiometric. The optimized parameters for the Mo-O system are reported in the work of Corcoran et al. [29]. The parameters for the liquid phase have been later updated in the PhD thesis of Kauric [30] to prevent the occurrence of a miscibility gap at very high MoO<sub>3</sub> content in ternary systems such as Cs-Mo-O or Na-Mo-O.

## 2.2. Structural data on the ternary Ba-Mo-O phases

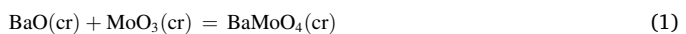
The Ba-Mo-O system is rather complex, with a number of ternary phases reported: BaMoO<sub>4</sub>, Ba<sub>2</sub>MoO<sub>5</sub>, Ba<sub>3</sub>MoO<sub>6</sub>, BaMo<sub>3</sub>O<sub>10</sub>, BaMo<sub>2</sub>O<sub>7</sub>, Ba<sub>2</sub>Mo<sub>5</sub>O<sub>17</sub>, Ba<sub>3</sub>Mo<sub>7</sub>O<sub>24</sub>, BaMoO<sub>3</sub>, Ba<sub>8</sub>/<sub>7</sub>Mo<sub>8</sub>O<sub>16</sub>, BaMo<sub>6</sub>O<sub>10</sub>, Ba<sub>3</sub>Mo<sub>18</sub>O<sub>28</sub>, and Ba<sub>5</sub>(Mo<sub>4</sub>O<sub>6</sub>)<sub>8</sub> (i.e. Mo at the valence states +3.71, +2.78, +2.69, respectively), were not included due to the lack of thermodynamic data, and because of the general scarcity of experimental information on the phase diagram equilibria in the regions of composition where such phases should be stable.

### 2.3. Thermodynamic data

Thermodynamic data in the literature are only available to the best of our knowledge on BaMoO<sub>4</sub>, BaMoO<sub>3</sub>, and BaMo<sub>2</sub>O<sub>7</sub>.

#### 2.3.1. BaMoO<sub>4</sub>

The enthalpy of formation of BaMoO<sub>4</sub> was determined by various authors using indirect measurement techniques and solution calorimetry. The values reported are summarized in Table 2. Tamman and Westerhold [40] derived the enthalpy of formation from the measurement of the enthalpy of reaction between barium oxide and molybdenum trioxide at  $T = 560$  K:



Lavrent'ev et al. obtained this data from the measurement of the oxygen potential of a phase mixture of BaO, Mo, and BaMoO<sub>4</sub> by equilibration with a mixture of H<sub>2</sub> and H<sub>2</sub>O in the temperature range  $T = (1473\text{--}1673)$

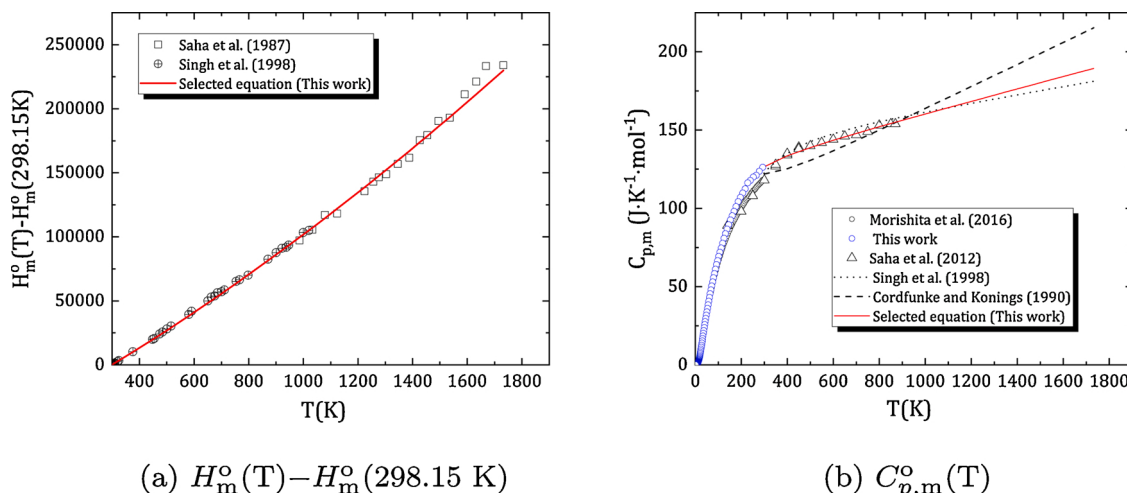
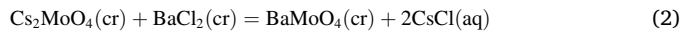


Fig. 2. (a) Enthalpy increments of BaMoO<sub>4</sub> and fit to the data. (b) Heat capacity of BaMoO<sub>4</sub> and fit to the data.

K [41]. However, the review of Cordfunke and Konings [42] suggested that equilibrium conditions were not reached during those experiments, explaining the discrepancy with other reported values. Rezukhina performed emf (electromotive force) measurements and studied reaction (Eq. (1)) [43]. Kubaschewski reviewed those measurements and derived  $\Delta_rH_m^o = -(208.4 \pm 10.5)$  kJ·mol<sup>-1</sup> for reaction (Eq. (1)). Combining with the enthalpies of formation of BaO and MoO<sub>3</sub> recommended by [42], we obtain an enthalpy of formation of BaMoO<sub>4</sub> of  $-(1501.4 \pm 10.7)$  kJ·mol<sup>-1</sup>. O'Hare [44] studied the precipitation of BaMoO<sub>4</sub>(cr) from an ammoniacal solution of BaCl<sub>2</sub>, and derived the enthalpy of formation based on the reaction:



Shukla et al. [45] also studied the precipitation of BaMoO<sub>4</sub>(cr), but from an ammoniacal solution of Ba(NO<sub>3</sub>)<sub>2</sub>, and derived the enthalpy of formation based on the reaction:



Singh et al. measured the standard molar Gibbs energy of formation of BaMoO<sub>4</sub> by measuring the emf of the cell {Pt/BaMoO<sub>3</sub>+BaMoO<sub>4</sub>/CSZ/air (p(O<sub>2</sub>) = 21.21 kPa, CSZ = 15 mol% CaO stabilized zirconia)} in the temperature range  $T = (1091\text{--}1309)$  K, and derived the standard enthalpy of formation by second and third law analyses of the data [46]. A more detailed description of the individual measurements can be found in [42], [45] and [46].

The values obtained by direct solution calorimetry measurements are preferred in this work. They are in good agreement and based on two different reaction schemes. Here we recommend the weighted<sup>1</sup> average of the aforementioned two values, i.e.  $\Delta_fH_m^o(\text{BaMoO}_4, \text{ cr}, 298.15\text{ K}) = -(1546.1 \pm 1.7)$  kJ·mol<sup>-1</sup>.

The low-temperature heat capacity was measured from 2.02 to 297.19 K using the thermal-relaxation method [49]. The heat capacity and the standard entropy at 298.15 K were determined in that study as  $C_{p,m}^o(\text{BaMoO}_4, \text{ cr}, 298.15\text{ K}) = 118.47 \text{ J}\cdot\text{K}^{-1}\cdot\text{mol}^{-1}$  and  $S_m^o(\text{BaMoO}_4, \text{ cr}, 298.15\text{ K}) = (152.69 \pm 1.53) \text{ J}\cdot\text{K}^{-1}\cdot\text{mol}^{-1}$ , respectively. The latter data were re-measured in this work using again the thermal-relaxation technique in the temperature range 2.1 to 293.2 K, which yielded higher values, namely  $C_{p,m}^o(\text{BaMoO}_4, \text{ cr}, 298.15\text{ K}) = (126.4 \pm 3.8) \text{ J}\cdot\text{K}^{-1}\cdot\text{mol}^{-1}$  and  $S_m^o(\text{BaMoO}_4, \text{ cr}, 298.15\text{ K}) = (160.4 \pm 3.8) \text{ J}\cdot\text{K}^{-1}\cdot\text{mol}^{-1}$ , respectively. The latter data are preferred and retained

for the thermodynamic model, for the reasons detailed in Section 5.3.

High temperature enthalpy increment measurements were reported using drop calorimetry in the temperature range  $T = (986\text{--}1732)$  K by Saha et al. [50], and in the temperature range  $T = (299\text{--}1020.3)$  K by Singh et al. [51]. From the data of Saha et al. [50], and constraining the fit to  $C_{p,m}^o(\text{BaMoO}_4, \text{ cr}, 298.15\text{ K}) = 122.2 \text{ J}\cdot\text{K}^{-1}\cdot\text{mol}^{-1}$ , Cordfunke and Konings [42] derived the equation:  $[H_m^o(T) - H_m^o(298.15\text{ K})]/\text{J}\cdot\text{mol}^{-1} = 91.9766(T/\text{K}) + 35.533410^{-3}(T/\text{K})^2 - 7.8535210^5(T/\text{K})^{-1} - 27947.5$ . Singh et al. [51] reported the following equation by constraining to the same heat capacity value at 298.15 K, and combining their data with that of Saha et al. [50]:  $[H_m^o(T) - H_m^o(298.15\text{ K})]/\text{J}\cdot\text{mol}^{-1} = 138.510(T/\text{K}) + 12.50910^{-3}(T/\text{K})^2 + 21.10110^5(T/\text{K})^{-1} - 49486$ . More recently, Saha et al. [52] reported direct measurements of the heat capacity of BaMoO<sub>4</sub> in the temperature range  $T = (140\text{--}870)$  K using Differential Scanning Calorimetry (DSC) and the step method. In this work, we have refitted the data of [50] and [51] using the constraints  $[H_m^o(T) - H_m^o(298.15\text{ K})]/\text{J}\cdot\text{mol}^{-1} = 0$  at 298.15 K and  $C_{p,m}^o(\text{BaMoO}_4, \text{ cr}, 298.15\text{ K}) = 126.4 \text{ J}\cdot\text{K}^{-1}\cdot\text{mol}^{-1}$ , which yielded:

$$C_{p,m}^o(\text{BaMoO}_4, \text{ cr}, T) / \text{J}\cdot\text{K}^{-1}\text{mol}^{-1} = 121.7475 + 3.918\cdot10^{-2}(T/\text{K}) - 6.248339\cdot10^5(T/\text{K})^{-2} \quad (4)$$

The latter equation is used for the thermodynamic model and compared in Figs. 2a and 7a to the experimental data, and selected equations by Cordfunke and Konings [42] and Singh et al. [51].

BaMoO<sub>4</sub> was reported to melt congruently at  $T = 1737$  K by Dash et al. [53], but the original source is not cited. It was moreover reported to melt at  $T = 1723$  K in the *Handbook of Inorganic Compounds* [54] based on the review by Knacke et al. [55]. A previous study by Ustinov et al. [56] reported a melting temperature at  $T = 1273$  K, but this is highly

**Table 3**  
Experimental measurements of the enthalpy of formation of BaMoO<sub>3</sub>(cr).

Reference	Method	$\Delta_fH_m^o(298.15\text{ K})$ (kJ·mol <sup>-1</sup> )
Zharkova and Barancheeva [42,60]	Oxygen Bomb calorimetry	$-(1228.1 \pm 15.3)$
Rezukhina and Levitskii [42,59]	EMF	$-(1225.5 \pm 10.3)$
Dash et al. [61]	Knudsen mass-loss – second law	$-(1257.5 \pm 3.6)$
	Knudsen mass-loss – third law	$-(1266.3 \pm 1.0)$
Cordfunke and Konings [42]	Review	$-(1227.0 \pm 15.0)$

<sup>1</sup> The weighted average was calculated as recommended by Guillaumont et al. for independent source data [48].

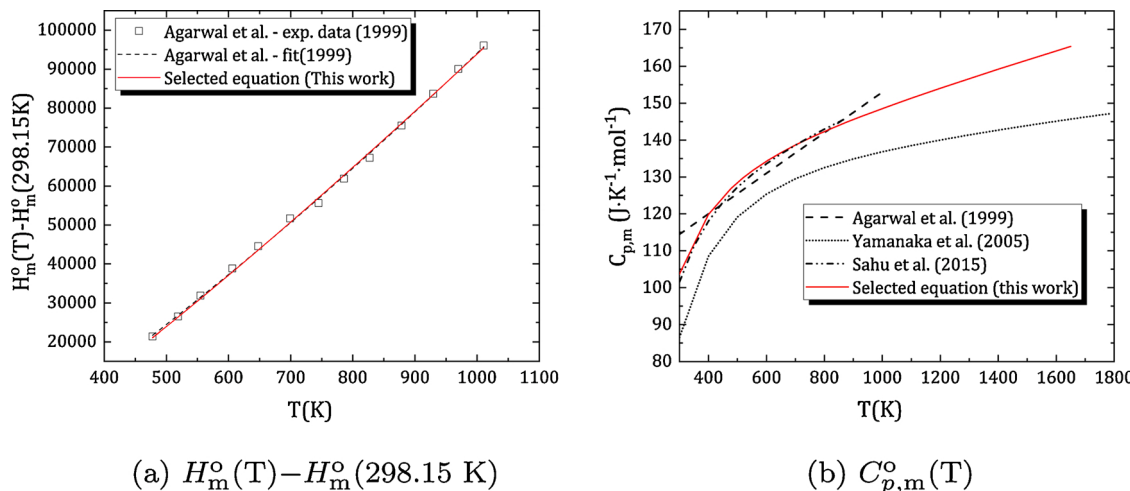


Fig. 3. (a) Enthalpy increments of BaMoO<sub>3</sub> and fit to the data. (b) Heat capacity of BaMoO<sub>3</sub> and fit to the data.

unlikely for the reasons detailed in Section 2.4. The enthalpy of fusion of BaMoO<sub>4</sub> was not reported in the literature. By comparison with other isostructural alkaline-earth molybdates and tungstates (CaMoO<sub>4</sub> and BaWO<sub>4</sub>), and assuming a constant fusion entropy for the series of isostructural compounds, one can expect this fusion enthalpy to be in the order of 94 to 102 kJ·mol<sup>-1</sup>. The fusion temperature and fusion enthalpy of CaMoO<sub>4</sub> were reported as (1750 ± 4) K and (102 ± 6) kJ·mol<sup>-1</sup> [57], respectively. The same data for BaWO<sub>4</sub> were found as 1775.1 K and 96.9 kJ·mol<sup>-1</sup> [58], respectively.

### 2.3.2. BaMoO<sub>3</sub>

The enthalpy of formation of BaMoO<sub>3</sub> was determined using the emf technique [59], oxygen bomb calorimetry [60] and Knudsen mass-loss method [61]. The values reported in the literature are summarized in Table 3. The values obtained by Dash et al. [61] by second and third laws are in good agreement, but about 35 kJ·mol<sup>-1</sup> lower than in the other studies. Here we prefer to retain the recommendation of Cordfunke and Konings [42] based on the average values of Zharkova et al. [60] and Rezukhina and Levitskii [59]:  $\Delta_f H_m^o(\text{BaMoO}_3, \text{cr}, 298.15\text{ K}) = -(1227.0 \pm 15.0) \text{ kJ}\cdot\text{mol}^{-1}$ .

There are no low-temperature heat capacity data available for this compound in the literature. Cordfunke and Konings [42] have estimated the heat capacity and entropy based on a comparison with BaZrO<sub>3</sub>:  $C_{p,m}^o(\text{BaMoO}_3, \text{cr}, 298.15\text{ K}) \sim (101.7 \pm 5.0) \text{ J}\cdot\text{K}^{-1}\cdot\text{mol}^{-1}$  and  $S_m^o(\text{BaMoO}_3, \text{cr}, 298.15\text{ K}) \sim (143.6 \pm 5.0) \text{ J}\cdot\text{K}^{-1}\cdot\text{mol}^{-1}$ , respectively. The entropy values reported by Rezukhina [43] and Rezukhina and Levitskii [59] based on emf studies are 119.43 and 92.04 J·K<sup>-1</sup>·mol<sup>-1</sup>, respectively. Dash et al. estimated 82.28 J·K<sup>-1</sup>·mol<sup>-1</sup> based on Knudsen effusion mass-loss measurements [61], while Yokokawa et al. [62] estimated 125.7 J·K<sup>-1</sup>·mol<sup>-1</sup>. It is clear that there is a large dispersion of reported values, and low-temperature heat capacity measurements are reported in this work to solve these discrepancies (see Section 5.3). The obtained data, selected for the present thermodynamic model, are  $C_{p,m}^o(\text{BaMoO}_3, \text{cr}, 298.15\text{ K}) = (103.4 \pm 3.1) \text{ J}\cdot\text{K}^{-1}\cdot\text{mol}^{-1}$  and  $S_m^o(\text{BaMoO}_3, \text{cr}, 298.15\text{ K}) = (111.3 \pm 2.8) \text{ J}\cdot\text{K}^{-1}\cdot\text{mol}^{-1}$ , respectively.

Agarwal et al. [63] reported enthalpy increment measurements in the temperature range  $T = (477.8\text{--}1010.8) K using a high temperature Calvet calorimeter. The fitting of this data [63] using the constraint  $[H_m^o(T) - H_m^o(298.15\text{ K})]/\text{J}\cdot\text{mol}^{-1} = 0$  at 298.15 K yielded:  $[H_m^o(T) - H_m^o(298.15\text{ K})]/\text{J}\cdot\text{mol}^{-1} = -31427 + 97.977(T/\text{K}) + 0.0275(T/\text{K})^2$ , and by derivation  $C_{p,m}^o(\text{BaMoO}_3, \text{cr}, T)/\text{J}\cdot\text{K}^{-1}\cdot\text{mol}^{-1} = 97.977 + 0.0550(T/\text{K})$ . The extrapolation of the latter equation to 298.15 K yields  $C_{p,m}^o(\text{BaMoO}_3, \text{cr}, 298.15\text{ K}) = 114.5 \text{ J}\cdot\text{K}^{-1}\cdot\text{mol}^{-1}$ , which is about$

11 J·K<sup>-1</sup>·mol<sup>-1</sup> higher than measured in this work. Yamanaka et al. [64] reported heat capacity measurements in the temperature range  $T = (300\text{--}1200)$  K using DSC with triple cells in a high purity argon atmosphere. The heat capacity was determined by both enthalpy and scanning methods at individual temperatures. Unfortunately the numerical values have not been listed in their paper. Only the fitted equation is given, i.e.  $C_{p,m}^o(\text{BaMoO}_3, \text{cr}, T)/\text{J}\cdot\text{K}^{-1}\cdot\text{mol}^{-1} = 131.8 + 9.36 \cdot 10^{-3}(T/\text{K}) - 4.33 \cdot 10^6(T/\text{K})^2$ . The extrapolation of the latter equation to 298.15 K yields 85.88 J·K<sup>-1</sup>·mol<sup>-1</sup>, which is much lower than expected, however. Sahu et al. [65] also reported heat capacity measurements in the temperature range  $T = (300\text{--}870)$  K using DSC and the step method. Here again, the numerical values have not been listed. Only the fitted equation is given:  $C_{p,m}^o(\text{BaMoO}_3, \text{cr}, T)/\text{J}\cdot\text{K}^{-1}\cdot\text{mol}^{-1} = 123.25 + 30 \cdot 10^{-3}(T/\text{K}) - 27.6 \cdot 10^5(T/\text{K})^2$ . The extrapolation of the latter equation to 298.15 K yields  $C_{p,m}^o(\text{BaMoO}_3, \text{cr}, 298.15\text{ K})/\text{J}\cdot\text{K}^{-1}\cdot\text{mol}^{-1} = 101.2 \text{ J}\cdot\text{K}^{-1}\cdot\text{mol}^{-1}$ , in good agreement with the data measured herein. The measurements of Agarwal et al. [63] and Sahu et al. [65] are compared in Fig. 3a and b. Both equations yield similar values above  $T = 450$  K, but differ largely on the extrapolation down to room temperature.

In this work, we have refitted the data of Agarwal et al. [63] and Sahu et al. [65] using the constraints  $[H_m^o(T) - H_m^o(298.15\text{ K})]/\text{J}\cdot\text{mol}^{-1} = 0$  at 298.15 K and  $C_{p,m}^o(\text{BaMoO}_3, \text{cr}, 298.15\text{ K}) = 103.4 \text{ J}\cdot\text{K}^{-1}\cdot\text{mol}^{-1}$  (obtained in this work), which yielded:

$$C_{p,m}^o(\text{BaMoO}_3, \text{cr}, T)/\text{J}\cdot\text{K}^{-1}\cdot\text{mol}^{-1} = 128.174 + 2.31710^{-2}(T/\text{K}) - 2.81632710^6(T/\text{K})^2 \quad (5)$$

The latter equation was implemented in our thermodynamic model.

Paschoal et al. [66] reported the decomposition of BaMoO<sub>3</sub> at  $T = 1653\text{ K}$  into BaMoO<sub>4</sub>(cr), Mo(cr) and BaO(g) according to Differential Thermal Analysis (DTA) measurements under argon and helium atmospheres, i.e. following the equilibrium reaction  $3\text{BaMoO}_3(\text{cr}) = 2\text{BaMoO}_4(\text{cr}) + \text{Mo}(\text{cr}) + \text{BaO}(\text{g})$ . More recently, Yamanaka et al. [64] measured the melting temperature of BaMoO<sub>3</sub> using a thermal arrest method under a reducing atmosphere and reported  $T_{fus}(\text{BaMoO}_3) = 1791\text{ K}$ . No enthalpy of fusion data are available to this date on this compound.

### 2.3.3. BaMo<sub>2</sub>O<sub>7</sub>

Singh et al. [67] measured the Gibbs energy of formation of BaMo<sub>2</sub>O<sub>7</sub> in the temperature range  $T = (828\text{--}985)$  K using an emf cell: {(-) Pt/BaMo<sub>2</sub>O<sub>7</sub>+BaMoO<sub>4</sub> +MoO<sub>2</sub>//CSZ//air (p(O<sub>2</sub>)=21.21 kPa)/Pt(+)} (CSZ = 0.15% calcia-stabilized zirconia)}. From a second law analysis of

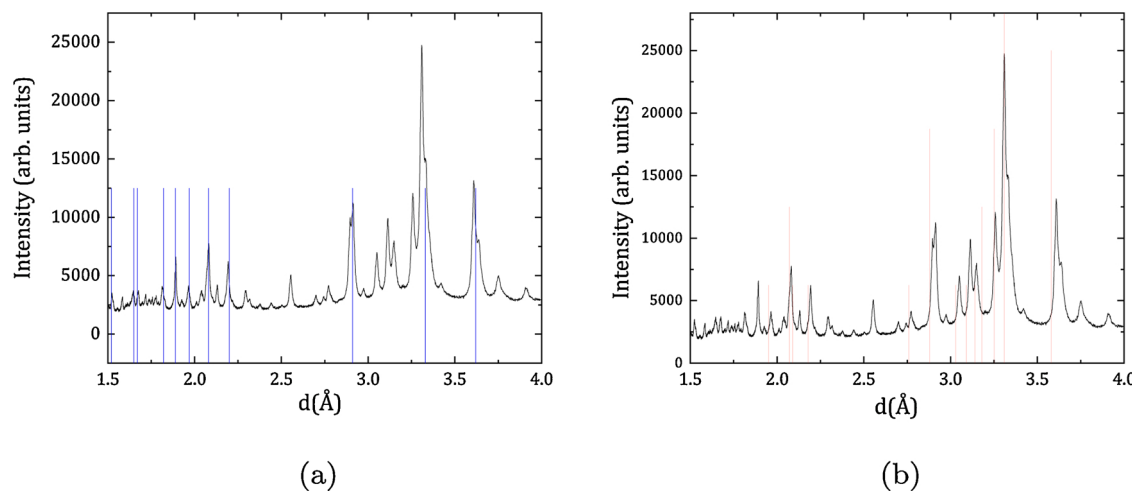


**Fig. 4.** Comparison of the interplanar spacings reported for the  $\text{BaMo}_2\text{O}_7$  phase by (a) Ustinov et al. [56] and (b) Zhukovskii et al. [69] with the X-ray diffraction pattern collected in this work for  $\text{BaMo}_3\text{O}_{10}$ .

their data, the authors derived the enthalpy of formation at 298.15 K as  $\Delta_f H_m^\circ(\text{BaMo}_2\text{O}_7, \text{cr}, 298.15 \text{ K}) = -(2291.2 \pm 2.5) \text{ kJ} \cdot \text{mol}^{-1}$ . The heat capacity was not measured to this date.

#### 2.4. Phase diagram data in the $\text{BaO}-\text{MoO}_3$ pseudo-binary section

There is no source in the literature reporting (to the best of our knowledge) a phase diagram over the complete composition range between  $\text{BaO}$  and  $\text{MoO}_3$ .  $\text{BaMoO}_4$  is found on the  $\text{BaO}-\text{MoO}_3$  pseudo-binary section at the composition  $x(\text{MoO}_3) = 0.5$ . Phase equilibrium data in the  $\text{BaO}-\text{BaMoO}_4$  section were reported by Yanushkevich and Zhukovskii [68], while a sketch of the  $\text{BaMoO}_4-\text{MoO}_3$  section was reported by Ustinov et al. [56] and Zhukovskii et al. [69]. However, the latter two sets of data are in rather poor agreement as seen in Fig. 12.

Yanushkevich and Zhukovskii studied the  $\text{BaO}-\text{BaMoO}_4$  section using X-ray and visual polythermal techniques [68] on  $\text{BaCO}_3-\text{MoO}_3$  mixtures after thermal treatment. Two intermediate compounds were identified on the pseudo-binary section, namely  $\text{Ba}_2\text{MoO}_5$  and  $\text{Ba}_3\text{MoO}_6$ , with transition temperatures  $T = 1573 \text{ K}$  (peritectic) and  $T \sim 1825 \text{ K}$  (congruent melting), respectively. In addition the authors found two eutectic equilibria, i.e. between  $\text{BaO}$  and  $\text{Ba}_3\text{MoO}_6$  around 1808 K, and between  $\text{Ba}_2\text{MoO}_5$  and  $\text{BaMoO}_4$  around 1493 K.

Ustinov et al. investigated the  $\text{BaMoO}_4-\text{MoO}_3$  phase diagram using thermography and X-ray diffraction [56] on  $(\text{BaO}:\text{MoO}_3)$  mixtures. The authors reported the existence of an incongruent melting compound of composition  $\text{BaMo}_2\text{O}_7$  (with a decomposition temperature around 988 K), and an eutectic equilibrium at  $x(\text{MoO}_3) = 0.811$  and  $T = 913 \text{ K}$ . The interplanar spacings reported for the  $\text{BaMo}_2\text{O}_7$  phase seem to match the  $\text{BaMo}_3\text{O}_{10}$  composition, however, as seen in Fig. 4a, where they are compared to the X-ray diffraction pattern collected in this work for  $\text{BaMo}_3\text{O}_{10}$ . Moreover, the authors also reported the melting temperature of  $\text{BaMoO}_4$  to be 1273 K, which is much lower than found in subsequent studies. The liquidus data on the  $\text{BaMoO}_4$  rich-side is therefore doubtful based on the latter result.

Zhukovskii et al. used thermal-optical, X-ray diffraction, and thermographic methods on  $(\text{BaO}:\text{MoO}_3)$  mixtures for their investigations [69]. The authors also claimed the existence of the  $\text{BaMo}_2\text{O}_7$  compound, but with a lower incongruent melting temperature, i.e.  $(926 \pm 3) \text{ K}$ . Again, the interplanar spacings listed for  $\text{BaMo}_2\text{O}_7$  are compared in Fig. 4b with the X-ray diffraction data collected in this work for  $\text{BaMo}_3\text{O}_{10}$ . Despite a general shift to lower angles, the  $d$  spacings seem to match rather well the  $\text{BaMo}_3\text{O}_{10}$  data. An eutectic equilibrium was also reported between  $\text{BaMo}_2\text{O}_7$  and  $\text{MoO}_3$  at  $x(\text{MoO}_3) = 0.8$  and  $T = (897 \pm 3) \text{ K}$ , in rather good agreement with the data of Ustinov et al.

[56].  $\text{BaMoO}_4$  was found stable up to at least 1673 K. The liquidus data found on the  $\text{BaMoO}_4$  rich-side were found much higher than in the studies of Ustinov et al., and seem more trustworthy based on the expected melting temperature of the barium molybdate.

#### 2.5. Thermodynamic modelling assessment

Dash et al. [53] reported a thermodynamic model for the  $\text{Ba}-\text{Mo}-\text{O}$  system using the SOLGASMIX-PV program [70]. The authors considered 9 compounds in this system:  $\text{BaMoO}_3$ ,  $\text{BaMoO}_4$ ,  $\text{BaMo}_2\text{O}_7$ ,  $\text{BaMo}_3\text{O}_{10}$ ,  $\text{BaMo}_4\text{O}_{13}$ ,  $\text{Ba}_2\text{MoO}_5$ ,  $\text{Ba}_2\text{Mo}_5\text{O}_{17}$ ,  $\text{Ba}_3\text{MoO}_6$ , and  $\text{Ba}_3\text{Mo}_7\text{O}_{24}$ . The Gibbs energy functions for the ternary phases were estimated using the additive oxide method for the standard entropy and enthalpy of formation, and using the rule of Neumann-Kopp for the heat capacity, when no experimental data were available in the literature. Only the computed isothermal section of the  $\text{Ba}-\text{Mo}-\text{O}$  phase diagram at  $T = 700 \text{ K}$  is shown in their work. The authors reported  $\text{O}_2(\text{g})$ ,  $\text{BaO}(\text{g})$ ,  $\text{BaMoO}_4(\text{g})$  and  $\text{BaMo}_3(\text{g})$  to be the predominant vapour species in all ternary phase fields, and over pure compounds. The authors also observed that the calculated oxygen potentials over the ternary phase fields and pure compounds were not affected much by the change of the Gibbs energy functions of the ternary phases. However, this had a more pronounced effect on the partial pressures of  $\text{Ba}(\text{g})$ ,  $\text{BaO}(\text{g})$ ,  $\text{BaMoO}_4(\text{g})$  and  $\text{BaMo}_3(\text{g})$  (one to two orders of magnitude). Experimental investigations of the stable ternary phase fields are needed to confirm the predictions of the computed phase diagram by [53], which are unfortunately not available to this date.

### 3. Experimental methods

#### 3.1. Sample preparation

$\text{BaMoO}_4$  was prepared by solid state reaction between accurately weighted quantities of barium carbonate ( $\text{BaCO}_3$ , >99%, Fluka) and molybdenum oxide ( $\text{MoO}_3$ , 99.95%, Sigma-Aldrich), heated under air in an alumina boat at 1023 K for 24 h with an intermediate regrinding step.  $\text{BaMoO}_3$  was subsequently obtained by reduction of the synthesized  $\text{BaMoO}_4$  material in  $\text{Ar}/\text{H}_2(5\%)$  flow at 1130 K for 12 h in a tubular furnace.  $\text{BaMo}_3\text{O}_{10}$  was synthesized by mixing  $\text{BaMoO}_4$  and  $\text{MoO}_3$  in stoichiometric ratio and heating in a platinum crucible under oxygen flow for 12 h at 823 K, followed by 2 h at 993 K. After regrinding, the sample was subjected to a second thermal treatment for 12 h at 823 K.

The purity of the synthesized materials was checked using X-ray diffraction. No secondary phases were detected, and the samples'

**Table 4**

Provenance and purity of the samples investigated in this study. XRD: X-ray diffraction; DSC: Differential Scanning Calorimetry.

Formula	Source	State	Color	Mass fraction purity	Purity analysis method
MoO <sub>3</sub>	Sigma-Aldrich	Powder	Light yellow/green	0.9995 ± 0.0005	Provided by supplier
BaCO <sub>3</sub>	Fluka	Powder	White	>0.99 ± 0.01	Provided by supplier
BaMoO <sub>4</sub>	Synthesized	Powder	White	0.99 ± 0.01	XRD
BaMoO <sub>3</sub>	Synthesized	Powder	Red	0.99 ± 0.01	XRD
BaMo <sub>3</sub> O <sub>10</sub>	Synthesized	Powder	White	0.99 ± 0.01	XRD, DSC

**Table 5**

Refined lattice parameters. X-ray diffraction measurements were performed at room temperature and atmospheric pressure. The derived standard uncertainties are given in parenthesis.

Phase	Symmetry	Space group	a/nm	b/nm	c/nm	$\beta/\text{°}$	$\rho/\text{g} \cdot \text{cm}^{-3}$
BaMoO <sub>4</sub>	Tetragonal	I4 <sub>1</sub> /a	0.55836(1)	0.55836(1)	1.28220(4)	90	4.9399(2)
BaMoO <sub>3</sub>	Cubic	Pm <sub>3</sub> m	0.40413(1)	0.40413(1)	0.40413(1)	90	7.0771(3)
BaMo <sub>3</sub> O <sub>10</sub>	Monoclinic	P2 <sub>1</sub>	1.4696(3)	0.7568(1)	0.6965(1)	100.43(1)	5.101(1)

purities is expected to be better than 99% [4].

### 3.2. Powder X-ray diffraction (XRD)

X-ray diffraction patterns were collected at room temperature using a PANalytical X'Pert PRO X-ray diffractometer mounted in the Bragg-Brentano configuration with a Cu anode (0.4 mm × 12 mm line focus, 45 kV, 40 mA), and the X-ray scattered intensities were measured with a real time multi strip (RTMS) detector (X'Celerator). The data were collected by step scanning in the angle range  $10^\circ \leq 2\theta \leq 120^\circ$  with a step size of 0.008° ( $2\theta$ ); total measuring time was about 8 h. Structural analysis was performed by the Rietveld method with the FullProf suite [71].

### 3.3. X-ray Absorption Near Edge Structure Spectroscopy (XANES)

XANES measurements were performed at the BM26A-DUBBLE BeamLine (Dutch-Belgian Beamline) of the European Synchrotron Radiation Facility (ESRF, Grenoble, France). Small amounts (10–20 mg) of powdered sample were mixed with boron nitride (BN), and pressed into pellets for the measurements. The storage ring operating conditions were 6.0 GeV and 170–200 mA. A double crystal monochromator mounted with a Si(111) crystal coupled to collimating and focusing Pt coated mirrors was used.

XANES spectra were collected at room temperature in transmission mode at the Mo K-edge. A step size of 1 eV was used in the edge region. The energy  $E_0$  of the edge absorption threshold position was taken at the inflection point of the spectrum by using the first node of the second derivative. The position of the pre-peak was selected from the first node of the first derivative. Several acquisitions were performed on the same sample and summed up to improve the signal-to-noise ratio. Before averaging the scans, each spectrum was aligned using the XANES spectrum of a metallic molybdenum reference foil measured before and after the series of samples under investigation (i.e. MoO<sub>2</sub>, Mo<sub>3</sub>, BaMoO<sub>3</sub>, and BaMoO<sub>4</sub>). The ATHENA software [72] was used to normalize the spectra.

### 3.4. Low-temperature heat capacity

Low-temperature heat capacity measurements were performed on BaMoO<sub>4</sub> ( $m = 12.25(5)$  mg) and BaMoO<sub>3</sub> ( $m = 40.63(5)$  mg) in the temperature ranges  $T = (2.1\text{--}293.2)$  K (BaMoO<sub>4</sub>), and  $T = (3.0\text{--}293.2)$  K (BaMoO<sub>3</sub>), respectively, using a PPMS (Physical Property Measurement System, Quantum Design) instrument, with no applied magnetic field ( $B = 0$  T). The samples were encapsulated in Stycast 2850 FT for the measurements ( $m_S = 2.87$  mg and  $m_S = 3.79$  mg for BaMoO<sub>4</sub> and BaMoO<sub>3</sub>, respectively), so as to improve the heat transfer with the

sample platform of these oxide materials. The heat capacity contribution of the Stycast was subtracted from the recorded data. This technique is based on a relaxation method, which was critically assessed by Lashley et al. [73]. The contributions of the sample platform, wires, and grease were deduced by a separate measurement of an addenda curve. Based on the experience acquired on this instrument with standard materials and other compounds, and the error associated with the encapsulation procedure in Stycast [74], the uncertainty was estimated at about 1–2% in the middle range of acquisition (from 10 to 70 K), and reaching about 3% at the lowest temperatures and near room temperature [73,74].

### 3.5. Differential Scanning Calorimetry (DSC)

The transition temperatures in the BaMoO<sub>4</sub>-MoO<sub>3</sub> pseudo-binary section of the Ba-Mo-O system were measured using simultaneous Thermogravimetry (TG)-Differential Scanning Calorimetry (DSC) measurements using plate type sensors in the TG-DSC module of the Setaram 96 Line calorimeter.

The temperatures were monitored throughout the experiments by a series of interconnected S-type thermocouples. The temperature on the heating ramp ( $10 \text{ K} \cdot \text{min}^{-1}$ ) was calibrated and corrected for the effect of the heating rate by measuring the melting points of standard high purity metals (In, Sn, Pb, Al, Ag, Au) at 2·4·6·8·10·12  $\text{K} \cdot \text{min}^{-1}$ . The calibration procedure was performed as recommended by Höne et al. [75] and Gatta et al. [76]. The transition temperatures in the BaMoO<sub>4</sub>-MoO<sub>3</sub> phase diagram were derived on the heating ramp as the onset temperature using tangential analysis of the recorded heat flow. The liquidus temperature of mixtures was derived from the peak extremum of the last thermal event. The uncertainty on the measured temperatures is estimated to be  $\pm 5$  K for pure compounds and  $\pm 10$  K for mixtures.

BaMoO<sub>4</sub> and MoO<sub>3</sub> were mixed together in the selected stoichiometric ratios by grinding at room temperature, and subsequently inserted in the calorimeter for measurement. In some cases, the mixtures were pre-treated under air at 800 K for 20 h before the TG-DSC measurement. The samples were placed in an alumina crucible on top of

**Table 6**

Energies of the pre-peaks and inflection points of the Mo K-edge XANES spectra.

Compound	Pre-peak (eV)	Inflection point $E_0$ (eV) <sup>a</sup>
Mo <sup>0</sup>		20000.0
Mo <sup>IV</sup> O <sub>2</sub>		20012.0
Mo <sup>V</sup> O <sub>3</sub>	20007.6	20015.7
BaMoO <sub>3</sub>		20011.8
BaMoO <sub>4</sub>	20006.1	20015.1

<sup>a</sup> The estimated expanded uncertainty (with a coverage factor  $k = 2$ ) on the energies is 1.0 eV.

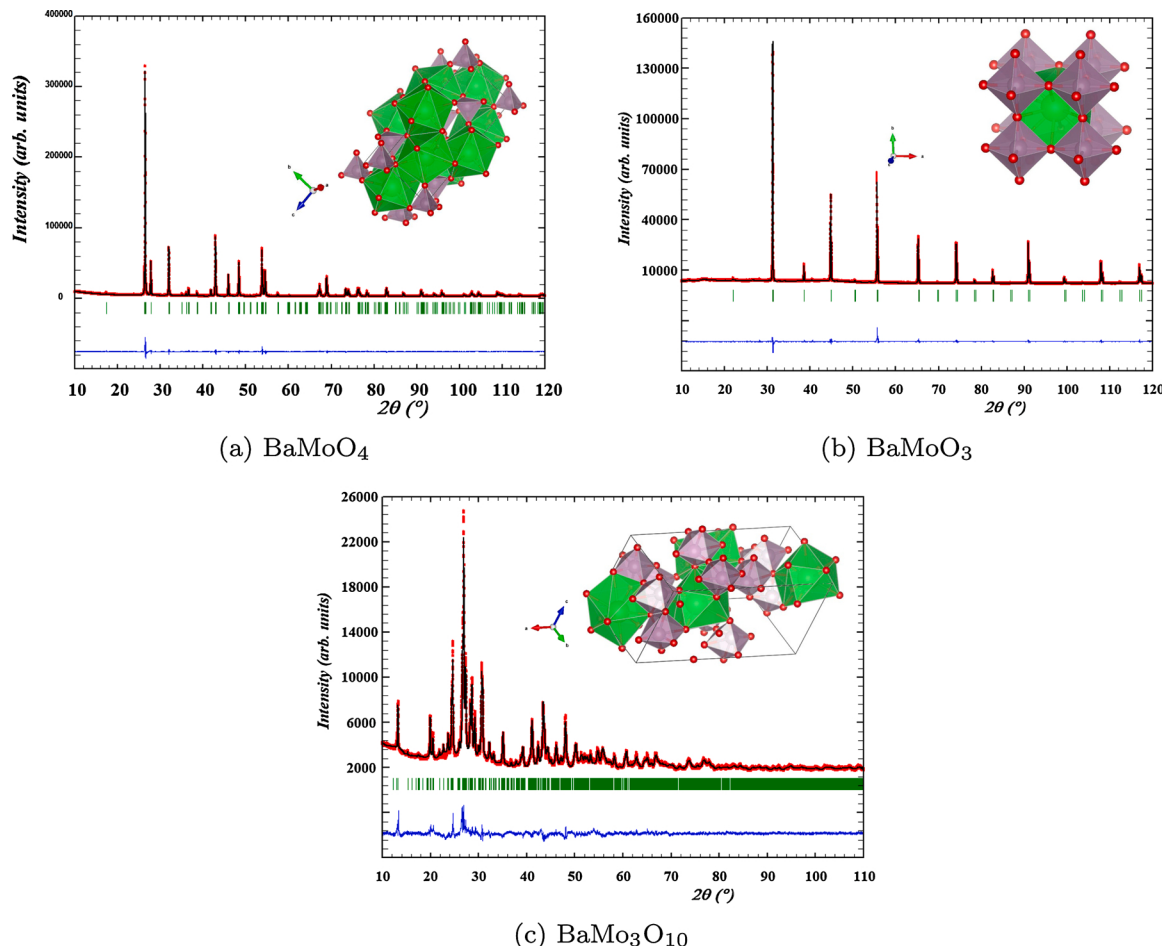


**Fig. 5.** Comparison between the observed ( $Y_{obs}$ , in red) and calculated ( $Y_{calc}$ , in black) X-ray diffraction patterns of (a) BaMoO<sub>4</sub>, (b) BaMoO<sub>3</sub>, and (c) BaMo<sub>3</sub>O<sub>10</sub>.  $Y_{obs} - Y_{calc}$ , in blue, is the difference between the experimental and calculated intensities. The Bragg reflections' angular positions are marked in green. Measurement at  $\lambda = \text{Cu-K}\alpha_1$ ,  $\lambda = 1.541 \text{ \AA}$ , Cu-K $\alpha_2$ ,  $\lambda = 1.544 \text{ \AA}$ . The corresponding unit cells are shown as inset with oxygen atoms in red, molybdenum polyhedra in purple and barium polyhedra in green. (For interpretation of the references to color in this figure legend, the reader is referred to the web version of this article.)

boron nitride powder to avoid chemical interactions with the crucible upon melting (which would lead to the formation of aluminium molybdate). They were measured under oxygen flow to avoid reduction of the MoO<sub>3</sub> to lower valence states molybdenum oxides. It should be noted that with the present measurement configuration, the data could be collected up to a maximum temperature of about 1173 K, due to excessive boron nitride oxidation above the latter temperature, which affected the shape of the heat flow baseline curve. One typical measurement consisted in three heating cycles with  $10 \text{ K} \cdot \text{min}^{-1}$  heating rate. The data collected on the first heating ramp were not considered for the analysis, however. The first heating cycle was used to equilibrate the samples, and the data collected in the subsequent two cycles were used for the analysis. The shape of the heat flow signal was mostly identical on the second and third cycles, indicating that thermodynamic equilibrium conditions were reached. After the TG-DSC measurements, selected samples were analysed using X-ray diffraction to confirm the nature of the observed transitions.

In addition, the enthalpy associated with the peritectic decomposition of BaMo<sub>3</sub>O<sub>10</sub> was determined in this work using the Multi HTC module of the same 96 Line allowing 3D-heat flow measurements. The enthalpy was determined by placing a reference material of well-known transition enthalpy in the reference crucible and measuring both sample and reference materials in the same cycle. This configuration allows to calculate for each individual measurement cycle the detector sensitivity equal to:

$$s_{ref} = \frac{M_{ref} \cdot A_{ref}}{m_{ref} \cdot \Delta_{tr} H_m^o(T_{tr,ref})} \quad (6)$$

where  $s_{ref}$  is the detector sensitivity in  $\mu\text{V} \cdot \text{mW}^{-1}$ ,  $M_{ref}$  the molar mass in  $\text{g} \cdot \text{mol}^{-1}$ ,  $m_{ref}$  the weight of the reference in mg,  $A_{ref}$  the peak area corresponding to the transition event in  $\mu\text{V} \cdot \text{s}$ , and  $\Delta_{tr} H_m^o(T_{tr,ref})$  the enthalpy of transition of the reference material in  $\text{J} \cdot \text{mol}^{-1}$ .

The detector sensitivity is assumed to remain the same at the temperature of the transition event of the sample, which is a reasonable approximation for two events sufficiently close to each other.

#### 4. Thermodynamic models

The thermodynamic parameters of the Ba-Mo-O CALPHAD model were optimized using the PARROT module of the Thermo-Calc software (Version 2016b) [77,78]. The hexavalent barium molybdates BaMoO<sub>4</sub>, Ba<sub>3</sub>MoO<sub>6</sub>, Ba<sub>2</sub>MoO<sub>5</sub>, BaMo<sub>2</sub>O<sub>7</sub>, and BaMo<sub>3</sub>O<sub>10</sub> were treated as stoichiometric compounds. BaMoO<sub>3</sub> was described with a more general formalism for a perovskite phase, compatible with the description of the grey-phase (Ba,Sr)(Zr,U,Mo)O<sub>3</sub> in the TAF-ID database [10]. The Gibbs energy functions of all the phases are referred to the enthalpy of the pure elements in their stable state at room temperature 298.15 K and 1 bar ( ${}^oH_i^{\text{SER}}(298.15 \text{ K})$ ). Note that the gas phase included in the present model was not optimized, and will be the subject of future works. The optimized parameters of the binary constituting sub-systems Ba-Mo and Ba-O can be found in Tables B.1, B.2, C.1, and C.2 .

#### 4.1. Pure elements

The Gibbs energy functions of the pure elements  $i$  at temperature  $T$  and in their state  $\varphi$  are given by:

$$G_i^\varphi(T) - {}^oH_i^{\text{SER}}(298.15\text{ K}) = a + b \cdot T + c \cdot T \cdot \ln T + \sum d_n T^n \quad (7)$$

where  $n$  is an integer (2, 3, -1...). The parameters reported by Dinsdale are used in this work for pure barium, molybdenum, and oxygen [79].

Metallic barium and molybdenum are included in the description of the BCC A2 phase with sublattices  $(\text{Ba},\text{Mo})(\text{O},\text{Va})_3$  ( $\text{Va}$  being a vacancy). The Gibbs energy functions of the  $(\text{Ba})(\text{Va})_3$  and  $(\text{Mo})(\text{Va})_3$  end-members are those of Dinsdale [79].

#### 4.2. Binary oxides

The binary oxides  $\text{BaO}_2$ ,  $\text{MoO}_2$ ,  $\text{Mo}_4\text{O}_{11}$ ,  $\text{Mo}_8\text{O}_{23}$ ,  $\text{Mo}_9\text{O}_{26}$ , and  $\text{MoO}_3$  are described as stoichiometric compounds. The corresponding Gibbs energy functions have the same form as in Eq. (7):

$$G^\varphi(T) - \sum_i n_i^\varphi {}^oH_i^{\text{SER}}(298.15\text{ K}) = a + b \cdot T + c \cdot T \cdot \ln T + \sum d_n T^n \quad (8)$$

where  $n_i^\varphi$  is the number of atoms of the  $i^{\text{th}}$  element in the oxide formula. These are taken from the TAF-ID database [10].

#### 4.3. Halite phase

The halite  $\text{BaO}$  is described with a two sublattice model  $(\text{Ba}^{2+},\text{Va})(\text{O}^{2-},\text{Va})$ , where  $\text{Va}$  are vacancies. The Gibbs energies of the end-members take the same form as in Eq. (7) and Eq. (8). No interaction parameter was introduced.

#### 4.4. Hexavalent ternary molybdates

The hexavalent ternary molybdates ( $\text{BaMoO}_4$ ,  $\text{Ba}_3\text{MoO}_6$ ,  $\text{Ba}_2\text{MoO}_5$ ,  $\text{BaMo}_2\text{O}_7$ , and  $\text{BaMo}_3\text{O}_{10}$ ), of general formula  $\text{Ba}_x\text{Mo}_y\text{O}_z$ , are described with a three-sublattice model of the form  $(\text{Ba}^{2+})_x(\text{Mo}^{6+})_y(\text{O}^{2-})_z$ . The Gibbs energy functions of the corresponding phases have the same form as in Eq. (7) and Eq. (8).

Experimental thermodynamic data are only available for the  $\text{BaMoO}_4$  scheelite phase as detailed in Section 2. The Gibbs energy for this phase has been expressed based on the recommended enthalpy of formation, standard entropy and heat capacity, and the enthalpic  $a$  and entropic  $b$  coefficients were subsequently optimized to fit the reported

congruent melting temperature and the rest of the thermodynamic and phase diagram data in the  $\text{BaO}-\text{MoO}_3$  section. For the other compounds, the Gibbs energies have been expressed as a function of  $\text{BaMoO}_4$  and the binary oxides  $\text{BaO}$  and  $\text{MoO}_3$ . The corresponding enthalpies of formation and entropies have been further optimized to fit the available phase diagram data in the  $\text{BaO}-\text{MoO}_3$  pseudo-binary section.

#### 4.5. $\text{BaMoO}_3$ perovskite

The descriptions adopted for the  $\text{BaUO}_3$  and  $\text{BaZrO}_3$  perovskites in the TAF-ID database is also adopted in this work for  $\text{BaMoO}_3$  to enable extrapolations to higher order systems, and the modelling of the multi-component grey-phase formed in irradiated fuel  $\text{Ba}(\text{Zr,U,Mo})\text{O}_3$ . A three-sublattice model is used with  $\text{Ba}^{2+}$  and  $\text{Mo}^{4+}$  cations on the second sublattice, i.e.  $(\text{Ba}^{2+})(\text{Mo}^{4+},\text{Ba}^{2+})(\text{O}^{2-})_3$ . The corresponding higher-order model for the grey-phase in the TAF-ID is  $(\text{Ba}^{2+})(\text{Zr}^{4+},\text{U}^{4+},\text{U}^{6+},\text{Mo}^{4+},\text{Ba}^{2+})(\text{O}^{2-})_3$ . The partial substitution of the  $\text{U}^{4+}$  by  $\text{Ba}^{2+}$  on the second sublattice allows to reproduce the stability of the perovskite along the  $\text{BaUO}_3-\text{Ba}_3\text{UO}_6$  tie-line in the  $\text{Ba-U-O}$  system [10]. The Gibbs energy functions of the  $(\text{Ba}^{2+})(\text{Mo}^{4+})(\text{O}^{2-})_3$  and  $(\text{Ba}^{2+})(\text{Ba}^{2+})(\text{O}^{2-})_3$  end-members take the same forms as Eq. (7) and Eq. (8).

#### 4.6. Liquid phase

An ionic two-sublattice model is used to describe the liquid phase [80], with  $\text{Ba}^{2+}$  and  $\text{Mo}^{4+}$  cations on the first sublattice, and  $\text{MoO}_4^{2-}$ ,  $\text{O}^{2-}$  anions, charged vacancies  $\text{Va}^{Q-}$ , neutral  $\text{MoO}_3$ , and neutral oxygen  $\text{O}$  on the second sublattice:

$$(\text{Ba}^{2+}, \text{Mo}^{4+})_P (\text{MoO}_4^{2-}, \text{O}^{2-}, \text{Va}^{Q-}, \text{MoO}_3, \text{O})_Q \quad (9)$$

$P$  and  $Q$  are equal to the average charge of the opposite sublattice:

$$\begin{aligned} Q &= 2y_{\text{Ba}^{2+}} + 4y_{\text{Mo}^{4+}} \\ P &= 2y_{\text{MoO}_4^{2-}} + 2y_{\text{O}^{2-}} + Qy_{\text{Va}^{Q-}} \end{aligned} \quad (10)$$

where  $y_{\text{Ba}^{2+}}$ ,  $y_{\text{Mo}^{4+}}$ ,  $y_{\text{MoO}_4^{2-}}$ ,  $y_{\text{O}^{2-}}$ , and  $y_{\text{Va}^{Q-}}$  are the site fractions of barium cations, molybdenum cations,  $\text{MoO}_4^{2-}$ , oxygen anions, and charged vacancies on the second sublattice, respectively.  $P$  and  $Q$  vary with composition via the site fractions so as to keep the phase electrically neutral.

The Gibbs energy of the liquid phase in this formalism is given by:

with

$$\begin{aligned} G^{\text{liquid}} &= y_{\text{Ba}^{2+}} y_{\text{MoO}_4^{2-}} {}^oG_{(\text{Ba}^{2+})_2(\text{MoO}_4^{2-})_2} + y_{\text{Ba}^{2+}} y_{\text{O}^{2-}} {}^oG_{(\text{Ba}^{2+})_2(\text{O}^{2-})_2} + Qy_{\text{Ba}^{2+}} y_{\text{Va}^{Q-}} {}^oG_{(\text{Ba}^{2+})_1(\text{Va}^{Q-})_2} + y_{\text{Mo}^{4+}} y_{\text{MoO}_4^{2-}} {}^oG_{(\text{Mo}^{4+})_2(\text{MoO}_4^{2-})_4} + y_{\text{Mo}^{4+}} y_{\text{O}^{2-}} {}^oG_{(\text{Mo}^{4+})_2(\text{O}^{2-})_4} \\ &+ Qy_{\text{Mo}^{4+}} y_{\text{Va}^{Q-}} {}^oG_{(\text{Mo}^{4+})_1(\text{Va}^{Q-})_4} + Qy_{\text{MoO}_3} {}^oG_{\text{MoO}_3} + Qy_{\text{O}^{2-}} {}^oG_{\text{O}^{2-}} + RT \left[ P \left( y_{\text{Ba}^{2+}} \ln y_{\text{Ba}^{2+}} + y_{\text{Mo}^{4+}} \ln y_{\text{Mo}^{4+}} \right) + Q \left( y_{\text{MoO}_4^{2-}} \ln y_{\text{MoO}_4^{2-}} + y_{\text{O}^{2-}} \ln y_{\text{O}^{2-}} + y_{\text{Va}^{Q-}} \ln y_{\text{Va}^{Q-}} \right. \right. \\ &\left. \left. + y_{\text{MoO}_3} \ln y_{\text{MoO}_3} + y_{\text{O}^{2-}} \ln y_{\text{O}^{2-}} \right) \right] + G^{\text{excess}} \end{aligned} \quad (11)$$

$$\begin{aligned} G^{\text{excess}} &= y_{\text{Ba}^{2+}} y_{\text{O}^{2-}} y_{\text{Va}^{Q-}} L^0_{(\text{Ba}^{2+})_P(\text{O}^{2-}, \text{Va}^{Q-})_Q} \\ &+ Qy_{\text{Ba}^{2+}} y_{\text{Mo}^{4+}} y_{\text{Va}^{Q-}}^2 L^0_{(\text{Ba}^{2+}, \text{Mo}^{4+})_P(\text{Va}^{Q-})_Q} + (y_{\text{Ba}^{2+}} - y_{\text{Mo}^{4+}}) L^1_{(\text{Ba}^{2+}, \text{Mo}^{4+})_P(\text{Va}^{Q-})_Q} \\ &+ y_{\text{O}^{2-}} y_{\text{MoO}_3} [L^0_{(0, \text{MoO}_3)}] \\ &+ y_{\text{Ba}^{2+}} y_{\text{MoO}_4^{2-}} y_{\text{O}^{2-}} L^0_{(\text{Ba}^{2+})_P(\text{MoO}_4^{2-}, \text{O}^{2-})_Q} + (y_{\text{MoO}_4^{2-}} - y_{\text{O}^{2-}}) L^1_{(\text{Ba}^{2+})_P(\text{MoO}_4^{2-}, \text{O}^{2-})_Q} \\ &+ y_{\text{Ba}^{2+}} y_{\text{MoO}_4^{2-}} y_{\text{MoO}_3} L^0_{(\text{Ba}^{2+})_P(\text{MoO}_4^{2-}, \text{MoO}_3)_Q} + (y_{\text{MoO}_4^{2-}} - y_{\text{MoO}_3}) L^1_{(\text{Ba}^{2+})_P(\text{MoO}_4^{2-}, \text{MoO}_3)_Q} \end{aligned} \quad (12)$$

${}^0G_{(Ba^{2+})_2(MoO_4^{2-})_2}$ ,  ${}^0G_{(Ba^{2+})_2(O^{2-})_2}$ ,  ${}^0G_{(Ba^{2+})_1(Va^{1-})_2}$ ,  ${}^0G_{(Mo^{4+})_2(MoO_4^{2-})_4}$ ,  ${}^0G_{(Mo^{4+})_2(O^{2-})_4}$ ,  ${}^0G_{(Mo^{4+})_1(Va^{1-})_4}$ ,  ${}^0G_{MoO_3}$ ,  ${}^0G_O$  are the reference terms corresponding to the Gibbs energies of barium molybdate  $BaMoO_4(l)$  (times two), barium oxide  $BaO(l)$  (times two), barium metal,  $Mo_6O_{16}(l)$ , molybdenum oxide  $MoO_2(l)$  (times two), molybdenum metal,  $MoO_3(l)$ , and pure oxygen. The Gibbs energy of the liquid phase also contains a configurational entropy term related to mixing of the species on the first and second sublattices. Finally, the excess Gibbs energy interaction parameters terms used in this model are  $L_{(Ba^{2+})_P(O^{2-}, Va^{Q-})_Q}^0$  for the  $Ba-BaO_2$  composition range,  $L_{(Ba^{2+}, Mo^{4+})_P(Va^{Q-})_Q}^0$  and  $L_{(Ba^{2+}, Mo^{4+})_P(Va^{Q-})_Q}^1$  for the  $Ba-Mo$  range,  $L_{(O, MoO_3)}^0$  for the  $MoO_3-O$  range,  $L_{(Ba^{2+})_P(MoO_4^{2-}, O^{2-})_Q}^0$  and  $L_{(Ba^{2+})_P(MoO_4^{2-}, O^{2-})_Q}^1$  for the  $BaO-BaMoO_4$  range, and  $L_{(Ba^{2+})_P(MoO_4^{2-}, MoO_3)_Q}^0$  and  $L_{(Ba^{2+})_P(MoO_4^{2-}, MoO_3)_Q}^1$  for the  $BaMoO_4-MoO_3$  range, respectively.

#### 4.7. Gas phase

The gas phase is described by an ideal mixture of ( $Ba$ ,  $Ba_2$ ,  $BaO$ ,  $Ba_2O$ ,  $Ba_2O_2$ ,  $Mo$ ,  $Mo_2$ ,  $MoO$ ,  $MoO_2$ ,  $MoO_3$ ,  $Mo_2O_6$ ,  $Mo_3O_9$ ,  $Mo_4O_{12}$ ,  $Mo_5O_{15}$ ,  $BaMoO_4$ ,  $O$ ,  $O_2$ ,  $O_3$ ) gaseous species. The Gibbs energy is

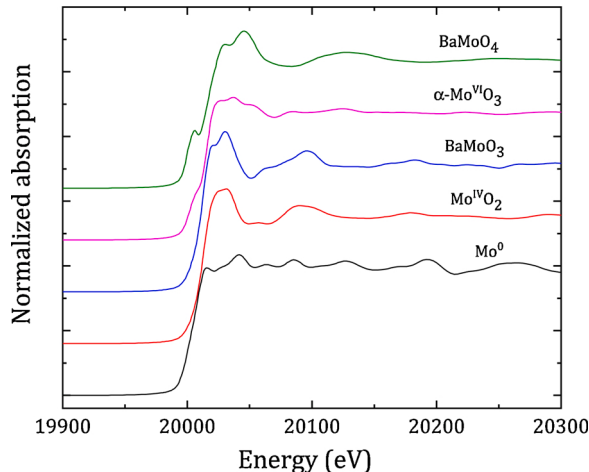


Fig. 6. Normalized XANES spectra of  $BaMoO_4$  and  $BaMoO_3$  together with  $Mo$ ,  $MoO_2$  and  $\alpha\text{-}MoO_3$  reference materials.

expressed by:

$$G^\varphi = \sum_i y_i {}^0G_i^\varphi + RT \sum_i y_i \ln y_i + RT \ln P / P^0 \quad (13)$$

where  $y_i$  is the fraction of the species  $i$  in the gas phase,  ${}^0G_i^\varphi$  the standard Gibbs energy of the gaseous species  $i$ , and  $P^0$  the standard pressure. The function for  $BaMoO_4$  is taken from the SGTE database [81]. Note that the computed pressures in the ternary system  $Ba-Mo-O$  are not commented in this work, and will be the subject of future work in our research group. We refer the reader to the Appendix for the expressions of the gaseous functions of the binary species.

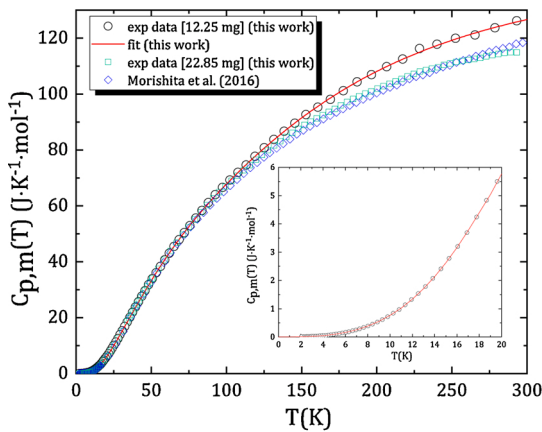
## 5. Experimental results and discussion

### 5.1. Structural analysis

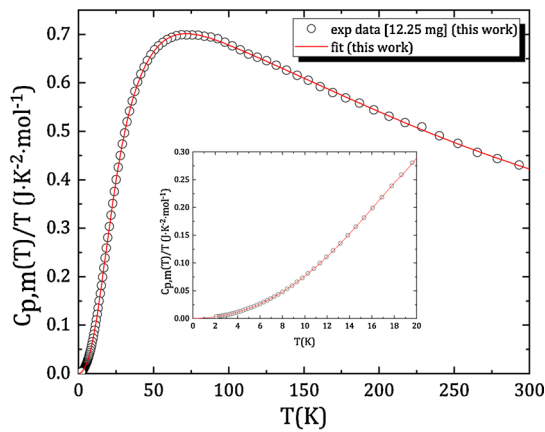
$BaMoO_4$ ,  $BaMoO_3$ , and  $BaMo_3O_{10}$  adopt a tetragonal, cubic, and monoclinic structure, respectively. The scheelite  $BaMoO_4$  crystallizes in space group  $I4_1/a$ .  $BaMoO_3$  shows a perovskite-type structure, in space group  $Pm\bar{3}m$ .  $BaMo_3O_{10}$  was reported with the space group  $P2_1$ . The refined cell parameters obtained by the Rietveld method from the XRD data are summarized in Table 5, and the X-ray diffraction patterns are shown in Fig. 5. The refined atomic positions are provided in the Supplementary Information.

### 5.2. Valence state determination by XANES: $BaMoO_4$ and $BaMoO_3$

The XANES spectra of  $BaMoO_4$  and  $BaMoO_3$  collected at the Mo K-edge are shown in Fig. 6 together with  $Mo^0$ ,  $Mo^{IV}O_2$ , and  $\alpha\text{-}Mo^{VI}O_3$  reference materials. The inflection point  $E_0$  positions (corresponding to the absorption edges) are listed in Table 6. The absorption edge of  $BaMoO_3$  is very close to that of  $Mo^{IV}O_2$ , while that of  $BaMoO_4$  is very well aligned with that of  $Mo^{VI}O_3$ , confirming the tetravalent and hexavalent valence states of molybdenum in those two materials, respectively. A shift of the inflection point to higher energy is observed with increasing valence state, as expected. In addition, the spectrum of  $BaMoO_4$  shows a characteristic pre-edge feature around 20006.1 eV of relatively high intensity. This is due to the presence of short and highly covalent Mo-O bonds in tetrahedral geometry in the latter compound (see Fig. 5a), which enhance  $4d$ - $5p$  mixing through their hybridization with  $O(2p)$  [82–84]. Similarly, a pre-edge shoulder appears in the spectrum of  $\alpha\text{-}MoO_3$  related to the distorted  $Mo_6$  octahedra in the structure (the  $1s(Mo) \rightarrow 4d(Mo) + 2p(O)$  transition is dipole-forbidden



(a)  $C_{p,m}$



(b)  $C_{p,m}/T$

Fig. 7. Heat capacity of  $BaMoO_4$  (○) measured in zero magnetic field and fit to the data (red line), and comparison with the data of Morishita et al. [49]. (For interpretation of the references to color in this figure legend, the reader is referred to the web version of this article.)

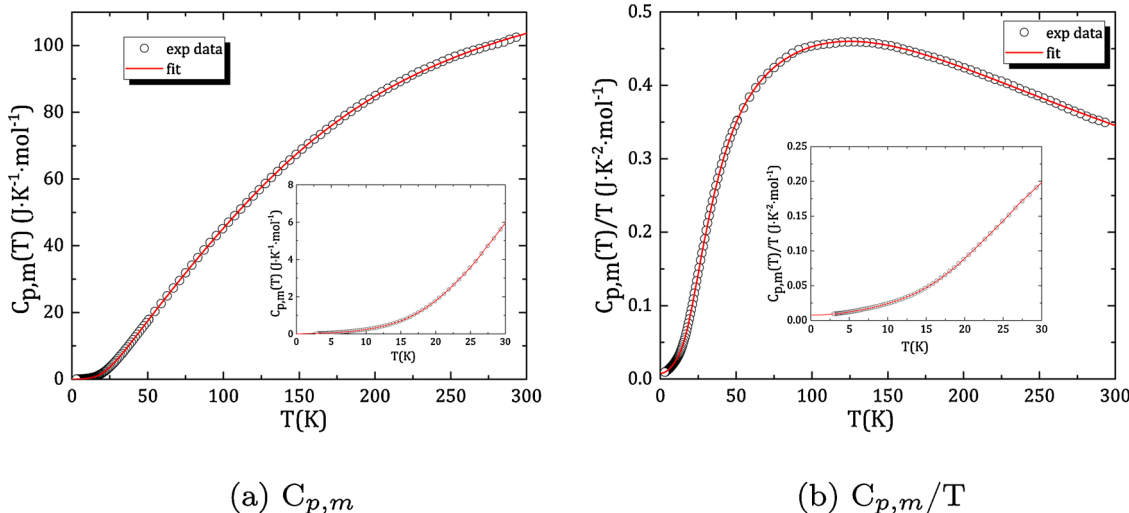


**Fig. 8.** Heat capacity of  $\text{BaMoO}_3$  ( $\circ$ ) measured in zero magnetic field and fit to the data (red line). (For interpretation of the references to color in this figure legend, the reader is referred to the web version of this article.)

**Table 7**  
Summary of fitting parameters of the heat capacity of  $\text{BaMoO}_4$  and  $\text{BaMoO}_3$ .

$\text{BaMoO}_4$			
Harmonic lattice-model		Debye and Einstein fit	
Temp. range/K	2.1–18.7	Temp. range/K	16.9–293.2
$\gamma/\text{mJ} \cdot \text{mol}^{-1} \cdot \text{K}^{-2}$	0	$n_D/\text{mol}$	1.8823
$B_3/\text{mJ} \cdot \text{mol}^{-1} \cdot \text{K}^{-4}$	$7.11831 \cdot 10^{-1}$	$\theta_D/\text{K}$	167.53
$B_5/\text{mJ} \cdot \text{mol}^{-1} \cdot \text{K}^{-6}$	$6.58781 \cdot 10^{-4}$	$n_{E1}/\text{mol}$	1.7521
$B_7/\text{mJ} \cdot \text{mol}^{-1} \cdot \text{K}^{-8}$	$-1.64151 \cdot 10^{-6}$	$\theta_{E1}/\text{K}$	284.95
		$n_{E2}/\text{mol}$	2.3319
		$\theta_{E2}/\text{K}$	650.78
		$n_D + n_{E1} + n_{E2}/\text{mol}$	5.97

$\text{BaMoO}_3$			
Harmonic lattice-model		Debye and Einstein fit	
Temp. range/K	1.9–26.6	Temp. range/K	24.9–293.2
$\gamma/\text{mJ} \cdot \text{mol}^{-1} \cdot \text{K}^{-2}$	7.71	$n_D/\text{mol}$	1.7140
$B_3/\text{mJ} \cdot \text{mol}^{-1} \cdot \text{K}^{-4}$	$1.86054 \cdot 10^{-1}$	$\theta_D/\text{K}$	239.40
$B_5/\text{mJ} \cdot \text{mol}^{-1} \cdot \text{K}^{-6}$	$-4.00474 \cdot 10^{-4}$	$n_{E1}/\text{mol}$	1.7122
$B_7/\text{mJ} \cdot \text{mol}^{-1} \cdot \text{K}^{-8}$	$2.34863 \cdot 10^{-6}$	$\theta_{E1}/\text{K}$	429.34
$B_9/\text{mJ} \cdot \text{mol}^{-1} \cdot \text{K}^{-10}$	$-3.95508 \cdot 10^{-9}$	$n_{E2}/\text{mol}$	1.6575
$B_{11}/\text{mJ} \cdot \text{mol}^{-1} \cdot \text{K}^{-12}$	$2.15708 \cdot 10^{-12}$	$\theta_{E2}/\text{K}$	721.21
		$n_D + n_{E1} + n_{E2}/\text{mol}$	5.08

for a perfectly regular  $\text{MoO}_6$  octahedron). A similar pre-peak feature has been reported in the literature for  $\text{Na}_2\text{MoO}_4$ ,  $\text{K}_2\text{MoO}_4$ , and  $\text{CaMoO}_4$  [84].

### 5.3. Standard entropy determination: $\text{BaMoO}_4$ and $\text{BaMoO}_3$

The low-temperature heat capacity data of  $\text{BaMoO}_4$  and  $\text{BaMoO}_3$  measured in the absence of magnetic field are shown in Figs. 2b and 8a, respectively, and are listed in the Supplementary Information. The heat capacity of both materials increases smoothly with temperature. The collected data do not exhibit any noticeable anomaly. The results for  $\text{BaMoO}_4$  are slightly higher than the data collected by Morishita et al. in the temperature range (2.02–297.19) K with the same relaxation

method. Two measurements were performed in this work for  $\text{BaMoO}_3$  with two different samples (12.25 mg and 22.85 mg, respectively). The data obtained with the 22.85 mg pellet were found in very good agreement with Morishita et al., but the other data were preferred for the reasons detailed hereafter. The data for  $\text{BaMoO}_3$  are reported for the first time in this work.

The thermodynamic functions of  $\text{BaMoO}_4$  and  $\text{BaMoO}_3$  were derived at 298.15 K by fitting the experimental data using the OriginPro 2015 software with the Levenbergh Marquardt iteration algorithm, using Origin C type fitting functions in the high temperature region, and simple expression type functions in the low-temperature region. The fitted data are shown with solid lines in Figs. 7a, 8a and 7b, 8b.

In the low-temperature region (below  $T = 15.7$  K for  $\text{BaMoO}_4$  and  $T = 26.6$  K for  $\text{BaMoO}_3$  in this case), the phonon contribution can be modelled using an harmonic-lattice model [85], as given by Eq. (14), where the number of required terms augments with the high temperature limit of the fit:

$$C_{\text{latt}} = \sum B_n T^n, \quad \text{where } n = 3, 5, 7, 9, \dots \quad (14)$$

The corresponding coefficients for  $\text{BaMoO}_4$  and  $\text{BaMoO}_3$  are listed in Table 7.

The electronic contribution of the conduction electrons at the Fermi surface are expressed with a linear term  $\gamma T$  [86]. The electronic specific heat of  $\text{BaMoO}_4$  is zero, as could be expected for such an insulating material. An electronic contribution of  $7.71 \text{ mJ} \cdot \text{mol}^{-1} \cdot \text{K}^{-2}$  is found for  $\text{BaMoO}_3$ . This is in good accordance with the study of Hayashi and Aoki [87], who reported metallic conductivity in the range (2.5 to 300) K based on resistivity measurements.

In the high-temperature region, the lattice contribution is modelled using a combination of Debye and Einstein functions [88], as expressed in Eq. (15). This method was used in the literature for several classes of inorganic materials: iron phosphates [89–91], zirconolite [92], calcium titanate [93], dicesium molybdate [94], double molybdates [95,96], alkali uranate and neptunate [97,98]. Two Einstein functions were used in combination with a Debye function. The fitted parameters are listed in Table 7. The sum  $(n_D + n_{E1} + n_{E2})$  is 5.97 and 5.08 for  $\text{BaMoO}_4$  and  $\text{BaMoO}_3$ , respectively. The same procedure applied to the 22.85 mg pellet of  $\text{BaMoO}_4$  gave a sum  $(n_D + n_{E1} + n_{E2})$  equal to 5.35, hence an underestimation compared to the 6 atoms expected from the formula unit. The measurement of very insulating materials as is the case for  $\text{BaMoO}_4$  is not always straightforward using the thermal-relaxation technique. The encapsulation procedure in Stycast has proved

**Table 8**

Equilibrium data collected by TG-DSC and DSC at pressure ( $0.10 \pm 0.01$ ) MPa on the heating ramp using a  $10 \text{ K} \cdot \text{min}^{-1}$  heating rate. Mixtures that were pre-treated under air at 800 K for 20 h before the TG-DSC measurements are indicated with an \*. The corresponding compositions in the BaO-MoO<sub>3</sub> pseudo-binary phase diagram is given by  $x(\text{MoO}_3)$ . \*\* Indicates a very minor impurity contamination. I indicates an unidentified impurity.

(BaMoO <sub>4</sub> :MoO <sub>3</sub> )	$x(\text{MoO}_3)$	$T_{eq}/\text{K}$	Equilibrium	Equilibrium reaction	Post-XRD
(0.59:0.41)	0.629	$894 \pm 10^{\text{a,c}}$	Peritectoid	$\text{BaMo}_2\text{O}_7 = \text{BaMoO}_4 + \text{BaMo}_3\text{O}_{10}$	$\text{BaMoO}_4 + \text{BaMo}_3\text{O}_{10} (+\text{MoO}_3^{**})$
	—	$915 \pm 10^{\text{a,c}}$	Peritectic	$\text{BaMo}_3\text{O}_{10} = \text{BaMoO}_4 + \text{Liq.}$	—
(0.539:0.461)	0.65	$894 \pm 10^{\text{a,c}}$	Peritectoid	$\text{BaMo}_2\text{O}_7 = \text{BaMoO}_4 + \text{BaMo}_3\text{O}_{10}$	$\text{BaMoO}_4 + \text{BaMo}_3\text{O}_{10} (+\text{MoO}_3^{**})$
	—	$917 \pm 10^{\text{a,c}}$	Peritectic	$\text{BaMo}_3\text{O}_{10} = \text{BaMoO}_4 + \text{Liq.}$	—
(0.5:0.5)*	0.6667	$887 \pm 10^{\text{a,c}*}$	Peritectoid	$\text{BaMo}_2\text{O}_7 = \text{BaMoO}_4 + \text{BaMo}_3\text{O}_{10}$	$\text{BaMoO}_4 + \text{BaMo}_3\text{O}_{10} (+\text{MoO}_3^{**}) + \text{I}^{**}$
	—	$914 \pm 10^{\text{a,c}*}$	Peritectic	$\text{BaMo}_3\text{O}_{10} = \text{BaMoO}_4 + \text{Liq.}$	—
(0.28:0.72)	0.781	$897 \pm 10^{\text{a,c}}$	Eutectic	$\text{BaMo}_3\text{O}_{10} + \text{Liq.} = \text{MoO}_3$	$\text{BaMo}_3\text{O}_{10} + \text{MoO}_3$
	—	$916 \pm 10^{\text{a,c}}$	Peritectic	$\text{BaMo}_3\text{O}_{10} + \text{Liq.} = \text{MoO}_3$	—
(0.25:0.75)	0.8	$888 \pm 10^{\text{a,c}}$	Eutectic	$\text{BaMo}_3\text{O}_{10} + \text{Liq.} = \text{MoO}_3$	$\text{BaMo}_3\text{O}_{10} + \text{MoO}_3$
	—	$915 \pm 10^{\text{b,d}}$	Liquidus	$\text{BaMo}_3\text{O}_{10} + \text{Liq.}' = \text{Liq.}$	—
(0.21:0.79)	0.826	$897 \pm 10^{\text{a,c}}$	Eutectic	$\text{BaMo}_3\text{O}_{10} + \text{Liq.} = \text{MoO}_3$	$\text{BaMo}_3\text{O}_{10} + \text{MoO}_3 + \text{I}$
	0.833	$892 \pm 10^{\text{a,c}*}$	Eutectic	$\text{BaMo}_3\text{O}_{10} + \text{Liq.} = \text{MoO}_3$	Not measured
(0.176:0.824)	0.85	$897 \pm 10^{\text{a,c}}$	Eutectic	$\text{BaMo}_3\text{O}_{10} + \text{Liq.} = \text{MoO}_3$	$\text{BaMo}_3\text{O}_{10} + \text{MoO}_3$
(0.15:0.85)	0.87	$895 \pm 10^{\text{a,c}}$	Eutectic	$\text{BaMo}_3\text{O}_{10} + \text{Liq.} = \text{MoO}_3$	Not measured
	—	$935 \pm 10^{\text{a,c}}$	Liquidus	$\text{BaMo}_3\text{O}_{10} + \text{Liq.}' = \text{Liq.}$	—
(0.11:0.89)	0.9	$886 \pm 10^{\text{a,c}}$	Eutectic	$\text{BaMo}_3\text{O}_{10} + \text{Liq.} = \text{MoO}_3$	$\text{BaMo}_3\text{O}_{10} + \text{MoO}_3$
	—	$966 \pm 10^{\text{a,c}}$	Liquidus	$\text{BaMo}_3\text{O}_{10} + \text{Liq.}' = \text{Liq.}$	—

<sup>a</sup> Data measured by TG-DSC.

<sup>b</sup> Data measured by DSC.

<sup>c</sup> Onset temperature of the heat flow signal.

<sup>d</sup> Peak maximum of the heat flow signal.

effective to improve the thermal coupling with the sample platform. Nevertheless, a too large weight in case of an insulator can lead to strong thermal inertia and long relaxation times, which reduces the accuracy of the results above  $\sim 250$  K. Because the fitting results obtained on the 12.25 mg pellet were found closer to the expected 6 atoms per formula unit than the results obtained on the 22.85 mg pellet, the former data were considered to be more reliable and were selected in this work. As a consequence, the retained heat capacity and entropy data for the thermodynamic assessment are higher than reported in the work of Morishita et al. [49]. It should be pointed out that the optimized standard entropy for BaMoO<sub>4</sub> in the thermodynamic model (see Section 6) is in very good agreement with the data selected herein. In fact, optimization of the thermodynamic model while constraining the heat capacity and standard entropy to values closer to that of Morishita et al. was also tested, but did not give as satisfactory results.

$$C_{p,m} = n_D D(\theta_D) + n_{E1} E(\theta_{E1}) + n_{E2} E(\theta_{E2}) \quad (15)$$

where  $D(\theta_D)$ ,  $E(\theta_{E1})$  and  $E(\theta_{E2})$  are the Debye and Einstein functions, respectively, as written in equations (16) and (17).  $\theta_D$ ,  $\theta_{E1}$ , and  $\theta_{E2}$  are the characteristic Debye and Einstein temperatures.  $n_D$ ,  $n_{E1}$ , and  $n_{E2}$  are adjustable parameters, whose sum ( $n_D + n_{E1} + n_{E2}$ ) should be approximately equal to the number of atoms in the formula unit (i.e., 6 and 5 in this case).

$$D(\theta_D) = 9R \left( \frac{T}{\theta_D} \right)^3 \int_0^{\theta_D/T} \frac{e^x x^4}{[e^x - 1]^2} dx \quad (16)$$

$$E(\theta_E) = 3Rx^2 \frac{e^x}{[e^x - 1]^2}, x = \frac{\theta_E}{T} \quad (17)$$

where  $R$  is the universal gas constant.

The heat capacity values at 298.15 K obtained by extrapolation are  $C_{p,m}^0(\text{BaMoO}_4, \text{cr}, 298.15 \text{ K}) = (126.4 \pm 3.8)^2 \text{ J} \cdot \text{K}^{-1} \cdot \text{mol}^{-1}$  and  $C_{p,m}^0(\text{BaMoO}_3, \text{cr}, 298.15 \text{ K}) = (103.4 \pm 3.1)^3 \text{ J} \cdot \text{K}^{-1} \cdot \text{mol}^{-1}$ . The

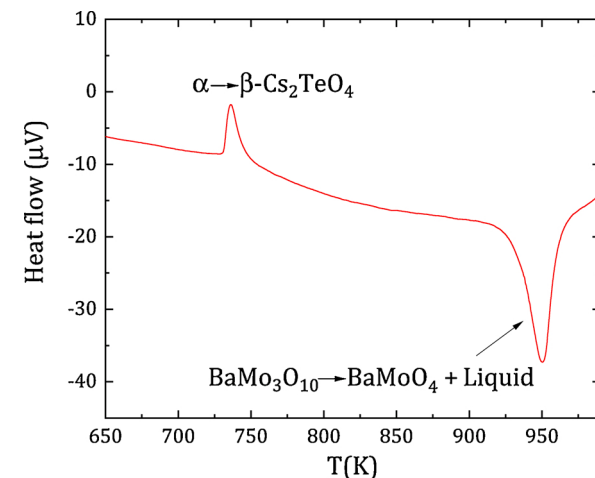


Fig. 9. DSC heat flow curve of BaMo<sub>3</sub>O<sub>10</sub> measured against a Cs<sub>2</sub>TeO<sub>4</sub> reference material.

experimental standard entropies at 298.15 K determined by numerical integration of  $(C_{p,m}/T) = f(T)$  using the aforementioned fitted functions, are  $S_m^0(\text{BaMoO}_4, \text{cr}, 298.15 \text{ K}) = (160.4 \pm 3.8)^4 \text{ J} \cdot \text{K}^{-1} \cdot \text{mol}^{-1}$  and  $S_m^0(\text{BaMoO}_3, \text{cr}, 298.15 \text{ K}) = (111.3 \pm 2.8)^5 \text{ J} \cdot \text{K}^{-1} \cdot \text{mol}^{-1}$ .

#### 5.4. Phase diagram measurements in the BaMoO<sub>4</sub>-MoO<sub>3</sub> pseudo-binary section

The transition temperatures in the BaMoO<sub>4</sub>-MoO<sub>3</sub> pseudo-binary section measured in this work by TG-DSC and DSC are listed in Table 8, and shown in Figs. 12 and 13. The corresponding thermograms are shown in Figs. A.1 and A.2 in the Appendix. No noticeable weight loss was observed from the thermogravimetry results, thus the initial

<sup>2</sup> The quoted uncertainty corresponds to the standard uncertainty.

<sup>3</sup> The quoted uncertainty corresponds to the standard uncertainty.

<sup>4</sup> The quoted uncertainty corresponds to the standard uncertainty.

<sup>5</sup> The quoted uncertainty corresponds to the standard uncertainty.

**Table 9**

Experimental results of the DSC measurements of  $\text{BaMo}_3\text{O}_{10}$  versus  $\text{Cs}_2\text{TeO}_4$  reference material. The quoted uncertainties correspond to standard uncertainties. They do not include systematic uncertainties.

$m_{\text{BaMo}_3\text{O}_{10}}$ (mg)	$m_{\text{Cs}_2\text{TeO}_4}$ (mg)	$A_{\text{sample}}$ ( $\mu\text{V} \cdot \text{s}$ )	$A_{\text{ref}}$ ( $\mu\text{V} \cdot \text{s}$ )	$s_{\text{ref}}$ ( $\mu\text{V} \cdot \text{mW}^{-1}$ )	$\Delta_{\text{tr}}H_m^{\circ}(\text{BaMo}_3\text{O}_{10},$ cr, $T_{\text{tr}}$ ) (kJ · mol $^{-1}$ )
28.1	101.2	2614.90	386.48	0.6540	$83.26 \pm 27.05$
21.5	91.8	1916.36	339.85	0.6345	$82.20 \pm 29.62$
<b>Average</b>					<b><math>82.8 \pm 20.0^a</math></b>

<sup>a</sup> The final averaged result  $X$  was calculated as a weighted mean using the formula  $X = \sum_i(X_i/\sigma_i^2)/\sum_i(1/\sigma_i^2)$ , while the uncertainty was calculated using the formula  $\sigma_X = \sqrt{\frac{1}{\sum_i(1/\sigma_i^2)}}$  as recommended in [48] considering that the individual measurements are independent source of data since fresh materials and crucibles were used each time.

**Table 11**

Optimized enthalpies of formation and standard entropies of the ternary barium molybdates. \*Values selected after critical review of the literature (see Section 2).

Compound	$\Delta_fH_m^{\circ}(298.15 \text{ K})$ (kJ · mol $^{-1}$ )		$S_m^{\circ}(298.15 \text{ K})$ (J · K $^{-1}$ · mol $^{-1}$ )	
	Optimized	Selected*	Optimized	Selected*
$\text{BaMo}_3$	-1262.0	-(1227.0 ± 15.0)	120.0	(111.3 ± 2.8)
$\text{BaMo}_4$	-1546.0	-(1546.1 ± 1.7)	160.3	(160.4 ± 3.8)
$\text{Ba}_3\text{Mo}_6$	-2788.4		277.2	
$\text{Ba}_2\text{Mo}_5$	-2166.2		223.7	
$\text{BaMo}_2\text{O}_7$	-2306.7	-(2291.2 ± 2.5)	226.4	
$\text{BaMo}_3\text{O}_{10}$	-3067.4		292.5	

**Table 10**

Summary of the thermodynamic data for pure elements and oxides selected in the present work. SER refers to the phase of the element stable at 298.15 K. The optimized coefficients are marked in bold.

Phase	Gibbs energy/(J · mol $^{-1}$ )	Ref.
Liquid	${}^oG(\text{Ba}^{2+})_2(\text{MoO}_4^{2-})_2 - 2{}^oH_{\text{Ba}}^{\text{SER}} - 2{}^oH_{\text{Mo}}^{\text{SER}} - 8{}^oH_O^{\circ} = 2G_{\text{BaMoO}_4} + \mathbf{193633} - 110.6T$ $L^0(\text{Ba}^{2+})_P(\text{MoO}_4^{2-}, \text{O}^{2-})_Q = - \mathbf{273954.6}$ $L^1(\text{Ba}^{2+})_P(\text{MoO}_4^{2-}, \text{O}^{2-})_Q = + \mathbf{30019.6}$ $L^0(\text{Ba}^{2+})_P(\text{MoO}_4^{2-}, \text{MoO}_3)_Q = - \mathbf{147769.0}$ $L^1(\text{Ba}^{2+})_P(\text{MoO}_4^{2-}, \text{MoO}_3)_Q = + \mathbf{58185.1}$	This work This work This work This work This work
Hexavalent molybdates	$G_{\text{BaMoO}_4} = - \mathbf{1586142.5} + \mathbf{670.34987}T - 121.7475T\ln(T) - 0.01959T^2 + 312416.95T^{-1}$ $G_{\text{Ba}_3\text{MoO}_6} = G_{\text{BaMoO}_4} + 2G_{\text{BaO}} - \mathbf{146274.2} + \mathbf{23.1}T$ $G_{\text{Ba}_2\text{MoO}_5} = G_{\text{BaMoO}_4} + G_{\text{BaO}} - \mathbf{72139.2} + \mathbf{6.6}T$ $G_{\text{BaMo}_2\text{O}_7} = G_{\text{BaMoO}_4} + G_{\text{MoO}_3} - \mathbf{16114.9} + \mathbf{11.563}T$ $G_{\text{BaMo}_3\text{O}_{10}} = G_{\text{BaMoO}_4} + 2G_{\text{MoO}_3} - \mathbf{32203.2} + \mathbf{23.0963}T$	This work This work This work This work This work
Perovskite	${}^oG(\text{Ba}^{2+})(\text{Mo}^{4+})(\text{O}^{2-})_3 - {}^oH_{\text{Ba}}^{\text{SER}} - {}^oH_{\text{Mo}}^{\text{SER}} - 3{}^oH_O^{\circ} = - \mathbf{1310690.918} + \mathbf{761.2069}T - 128.174T\ln(T) - 0.011585T^2 + 1408163.99T^{-1}$ ${}^oG(\text{Ba}^{2+})(\text{Ba}^{2+})(\text{O}^{2-})_3 - 2{}^oH_{\text{Ba}}^{\text{SER}} - 3o_O^{\text{HSER}} = + 2G_{\text{BaO}} + G_O^{\text{SER}} + 100000$	This work
Gas Functions	$G_{\text{BaMoO}_4}^{\text{gas}} - {}^oH_{\text{Ba}}^{\text{SER}} - {}^oH_{\text{Mo}}^{\text{SER}} - 4{}^oH_O^{\circ} = G_{\text{BaMoO}_4}^{\text{gas}} + RT\ln(10^{-5}P)$ $G_O^{\text{SER}} = 1/2{}^oG_{\text{O}_2}^{\circ}$ $G_{\text{Ba}}^{\text{SER}} = 17685.226 + 233.78606T - 42.889T\ln(T) - 0.0018314T^2 - 9.5 \cdot 10^{-11}T^3 + 705880T^{-1}(298 < T/K < 1000 K)$ $= -64873.614 + 608.188389T - 94.2824199T\ln(T) + 0.019504772T^2 - 1.051353 \cdot 10^{-6}T^3 + 8220192T^{-1}(1000 < T/K < 2995 K)$ $G_{\text{Mo}}^{\text{SER}} = -7746.302 + 131.9197T - 23.56414T\ln(T) - 0.003443396T^2 + 5.66283 \cdot 10^{-7}T^3 + 65812T^{-1} - 1.30927 \cdot 10^{-10}T^4(298 < T/K < 2896 K)$ $G_{\text{BaO}} = -562498.08 + 228.7677T - 43.56097T\ln(T) - 0.01114T^2 + 2.3824667 \cdot 10^{-6}T^3 - 2.5271667 \cdot 10^{-10}T^4 + 88016.981T^{-1}(298 < T < 2280 K)$ $= -568509.864 + 310.40284T - 55.84644T\ln(T) + 2T^{-9}(2280 < T < 6000 K)$ $G_{\text{MoO}_3} = -770709.73 + 429.56532T - 73.51818T\ln(T) - 0.01744741T^2 - 8.33756833 \cdot 10^{-10}T^3 + 393450.8T^{-1}(298 < T < 6000 K)$ $G_{\text{BaMoO}_4}^{\text{gas}} = -1014744.05 + 464.986607T - 122.198T\ln(T) - 0.00521535T^2 + 4.32346667 \cdot 10^{-7}T^3 + 1172955T^{-1}$	[81] [79] [79] [79] [26] [10] [81]

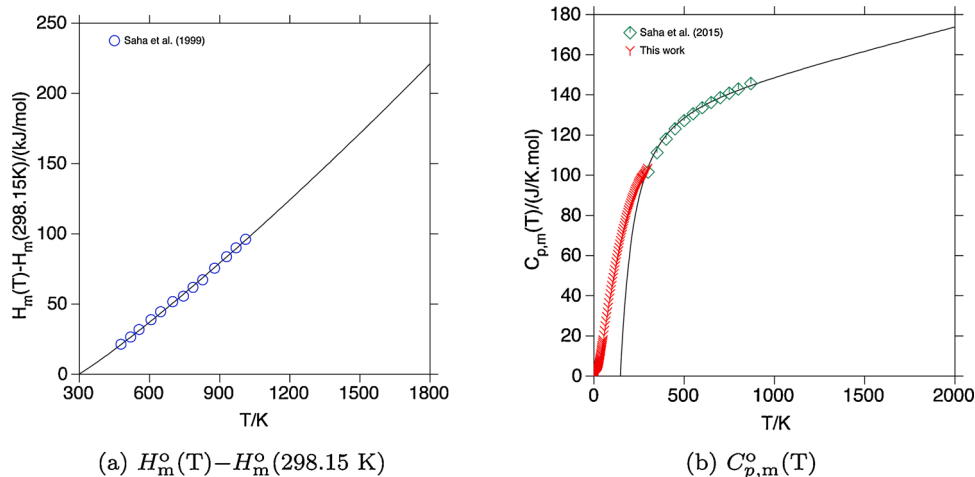
targeted composition should not have shifted during the measurement due to vaporization processes. Taken into account the uncertainty associated with the temperature calibration procedure, the final uncertainty on the measured temperatures is estimated to be  $\pm 10$  K.

The measured data were interpreted with an eutectic equilibrium at  $\{T \sim 893 \text{ K and } x(\text{MoO}_3) = 0.83\}$ . A single event was observed for the samples of compositions  $x(\text{MoO}_3) = 0.826$  and 0.833. Moreover,  $\text{BaMo}_3\text{O}_{10}$  ( $x(\text{MoO}_3) = 0.75$ ) is suggested to decompose in a peritectic reaction. The measured equilibria points around  $T \sim 892 \text{ K}$  are attributed to the peritectoid decomposition of  $\text{BaMo}_2\text{O}_7$ . The latter interpretation is based on a limited number of measured points. To confirm this interpretation, complementary measurements coupled with post-XRD and

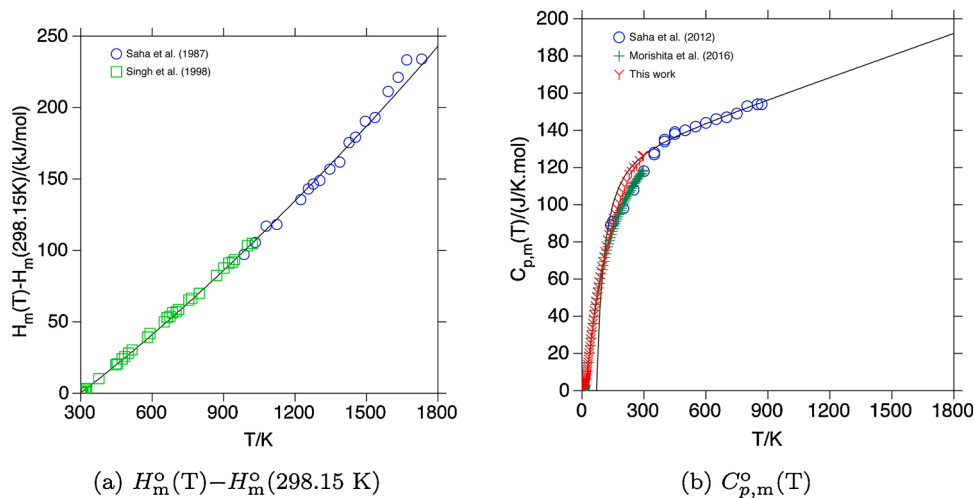
microscopic characterizations would be very valuable. It is worth pointing out that the reported decomposition temperature of  $\text{BaMo}_2\text{O}_7$  by Zhukovskii et al. [69] matches well the measured peritectic decomposition of  $\text{BaMo}_3\text{O}_{10}$ .

### 5.5. Transition enthalpy determination: $\text{BaMo}_3\text{O}_{10}$

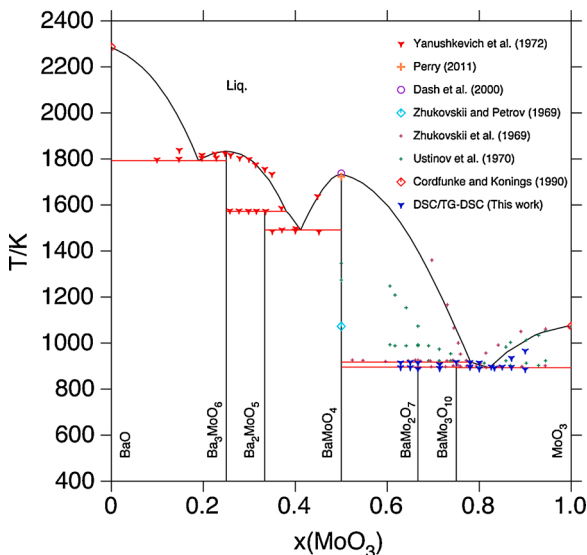
The decomposition temperature and enthalpy associated with the peritectic decomposition of  $\text{BaMo}_3\text{O}_{10}$  was determined using Differential Scanning Calorimetry. The average transition temperature over four heating cycles yielded  $(918 \pm 5)$  K. In addition, the enthalpy of transition was estimated by measuring  $\text{BaMo}_3\text{O}_{10}$  together with  $\text{Cs}_2\text{TeO}_4$



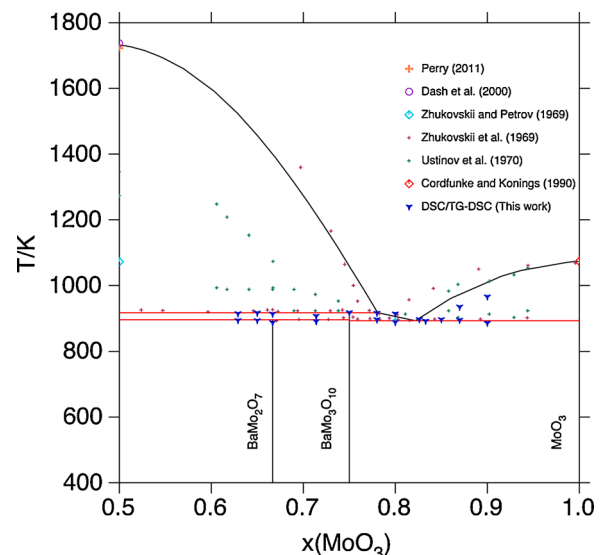
**Fig. 10.** (a) Enthalpy increments of BaMoO<sub>3</sub> measured experimentally and calculated in the model. (b) Heat capacity of BaMoO<sub>3</sub> measured experimentally and calculated in the model.



**Fig. 11.** (a) Enthalpy increments of BaMoO<sub>4</sub> measured experimentally and calculated in the model. (b) Heat capacity of BaMoO<sub>4</sub> measured experimentally and calculated in the model.



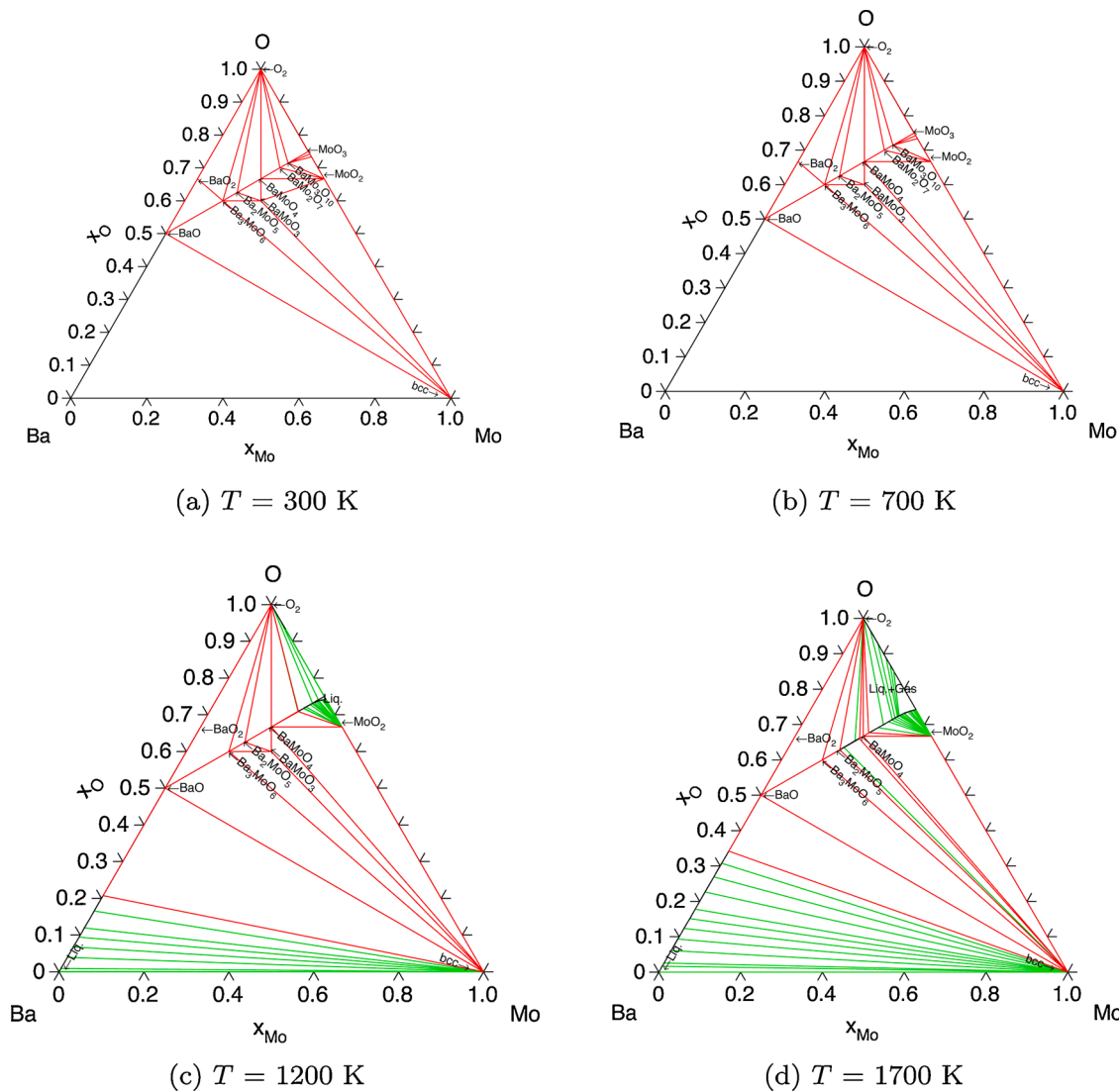
**Fig. 12.** BaO-MoO<sub>3</sub> pseudo-binary phase diagram computed from the thermodynamic model, and comparison with the experimental data.



**Fig. 13.** BaMoO<sub>4</sub>-MoO<sub>3</sub> pseudo-binary phase diagram computed from the thermodynamic model, and comparison with the experimental data.

**Table 12**Invariant equilibria calculated from the CALPHAD model in the BaO-MoO<sub>3</sub> pseudo-binary section.

Invariant equilibrium	Equilibrium type	CALPHAD model		Exp. data		Ref.
		x(MoO <sub>3</sub> )	T/K	x(MoO <sub>3</sub> )	T/K	
BaO + Ba <sub>3</sub> MoO <sub>6</sub> = Liquid	Eutectic	0.19	1794	0.175 <sup>a</sup>	1808 ± 10	[68]
Ba <sub>3</sub> MoO <sub>6</sub> = Liquid	Congruent melting	0.25	1833	0.25	~1825 <sup>a</sup> ± 10	[68]
Ba <sub>2</sub> MoO <sub>5</sub> = Ba <sub>3</sub> MoO <sub>6</sub> + Liquid	Peritectic	0.3333	1572	0.3333	1573 ± 10	[68]
Ba <sub>2</sub> MoO <sub>5</sub> + BaMoO <sub>4</sub> = Liquid	Eutectic	0.412	1492	0.4 <sup>a</sup>	1493 ± 10	[68]
BaMoO <sub>4</sub> = Liquid	Congruent melting	0.5	1734	0.5	1723, 1730	[54,53]
BaMo <sub>2</sub> O <sub>7</sub> = BaMoO <sub>4</sub> + BaMo <sub>3</sub> O <sub>10</sub>	Peritectoid	0.6667	892	0.6667	894 ± 5	This work
BaMo <sub>3</sub> O <sub>10</sub> = BaMoO <sub>4</sub> + Liquid	Peritectic	0.75	917	0.75	917.9 ± 5	This work
BaMo <sub>3</sub> O <sub>10</sub> + MoO <sub>3</sub> = Liquid	Eutectic	0.822	893	0.825	897.3 ± 10	This work

<sup>a</sup> The exact temperature or composition were not reported in the original publication, but read from the reported phase diagram.**Fig. 14.** Isothermal sections of the Ba-Mo-O system at (a) T = 300 K, (b) T = 700 K, (c) T = 1200 K, and (d) T = 1700 K.

reference material, whose enthalpy of transition was determined in another work in our research group as  $\Delta_{\text{tr}}H_{\text{m}}^{\circ}(\text{Cs}_2\text{TeO}_4, \text{cr}, T_{\text{tr}}) = (2.67 \pm 0.14) \text{ kJ} \cdot \text{mol}^{-1}$  [99]. Cs<sub>2</sub>TeO<sub>4</sub> was chosen as it displays a transition temperature close to the peritectic transition of BaMo<sub>3</sub>O<sub>10</sub>, but without overlapping. Moreover, both reference and sample being oxide materials, they are expected to show similar thermal properties (heat capacity and thermal conductivity). The curve of the recorded heat flow versus temperature for the latter measurement is shown in Fig. 9.

The first single peak corresponds to the polymorphic transition of Cs<sub>2</sub>TeO<sub>4</sub> (from an orthorhombic  $\alpha$  phase to an hexagonal  $\beta$  phase [99]) and the second peak to the peritectic decomposition of BaMo<sub>3</sub>O<sub>10</sub>. Note that the opposite directions for both (endothermic) events is due to the different positioning in the reference and sample crucibles, respectively.

Two measurements were performed on fresh material and averaged, yielding an enthalpy of transition equal to  $\Delta_{tr}H_m^o(\text{BaMo}_3\text{O}_{10}, \text{cr}, T_{tr}) = (82.8 \pm 20.0)^6 \text{ kJ} \cdot \text{mol}^{-1}$ . The results of the individual cycles are listed in Table 9. The reported uncertainties on the individual measurements are standard uncertainties. They include the uncertainty on the transition enthalpy of the reference material ( $\text{Cs}_2\text{TeO}_4$ ) combined with the uncertainty associated with the choice of the baseline for the peak integration (linear, spline, or tangential sigmoid).

## 6. Thermodynamic modelling assessment

### 6.1. Optimized parameters

A summary of the optimized parameters for the Ba-Mo-O system is given in Table 10.

### 6.2. Thermodynamic data

The standard enthalpies of formation and standard entropies at 298.15 K optimized in this work are listed in Table 11. The values for  $\text{BaMoO}_4$  are in good agreement with the selected values from the literature review (see Section 2) considering the reported uncertainties. The optimized enthalpy of formation and standard entropy of  $\text{BaMoO}_3$  are higher than recommended from the literature review, however. Such high values appeared necessary to match the decomposition temperature of this compound (calculated at  $T = 1660$  K and reported at  $T = 1653$  K by Paschoal et al. [66]). Since neither the enthalpy of formation nor the decomposition temperature for this compound are known with certitude, complementary measurements would be very valuable for the improvement of the thermodynamic model.

The calculated enthalpy increments and heat capacities of the same compounds are shown in Figs. 10a, 10 b, 11 a and 11 b. The agreement with the experimental data is very good. Note that the reported heat capacity equations are only valid above 298.15 K, and match the imposed constraints on  $C_{p,m}^o(298.15 \text{ K})$ , as selected from the literature review.

In addition, the calculated transition enthalpy for the peritectic decomposition of  $\text{BaMo}_3\text{O}_{10}$  is  $\Delta_{tr}H_m^o(T_{tr}) = 80.1 \text{ kJ} \cdot \text{mol}^{-1}$ , in very good agreement with the data measured in this work (i.e.  $82.8 \pm 20.0 \text{ kJ} \cdot \text{mol}^{-1}$ ). The transition enthalpy associated with the congruent melting of  $\text{BaMoO}_4$  is  $99.7 \text{ kJ} \cdot \text{mol}^{-1}$ , which is a reasonable value compared to the reported data for the isostructural  $\text{CaMoO}_4$  ( $102 \pm 6 \text{ kJ} \cdot \text{mol}^{-1}$  [57]) and  $\text{BaWO}_4$  ( $96.9 \text{ kJ} \cdot \text{mol}^{-1}$  [58]) compounds.

### 6.3. Phase diagram data

The calculated pseudo-binary section  $\text{BaO}-\text{MoO}_3$  is shown in Fig. 12 and compared with the available phase diagram data.

The agreement with the data of Yanushkevich et al. [68] in the  $\text{BaO}-\text{BaMoO}_4$  section, and the data measured in the  $\text{BaMoO}_4-\text{MoO}_3$  section in this work and by Zhukovskii et al. [69], is generally good. The calculated invariant equilibria are listed in Table 12.  $\text{Ba}_3\text{MoO}_6$  and  $\text{BaMoO}_4$  melt congruently at  $T = 1833$  K and  $T = 1734$  K, respectively.  $\text{Ba}_2\text{MoO}_5$  undergoes a peritectic decomposition at  $T = 1572$  K, and  $\text{BaMo}_3\text{O}_{10}$  a peritectic decomposition at  $T = 917$  K.  $\text{BaMo}_2\text{O}_7$  is suggested to undergo a peritectoid decomposition at  $T = 892$  K. The crystal structure of this compound remains unknown, however, and the post-XRD characterizations did not seem to indicate the presence of such a phase, by contrast with the measured calorimetric heat flow signals. Its existence thus still needs confirmation. The liquidus line

between  $\text{BaO}$  and  $\text{BaMoO}_4$  follows rather well the data of Yanushkevich et al. [68]. The situation on the  $\text{BaMoO}_4-\text{MoO}_3$  section is more complex. The liquidus line is in good agreement with the results of Zhukovskii et al. [69] up to  $x(\text{MoO}_3) \sim 0.8$ . In the  $\text{MoO}_3$ -rich region of the phase diagram, the liquidus line falls in between our data and that of Zhukovskii et al. [69] and Ustinov et al. [56]. Complementary measurements in the  $\text{BaMoO}_4-\text{MoO}_3$  section, and more specifically of the liquidus line would be very valuable to ascertain the phase equilibria in this region and solve the discrepancy between the three sets of data.

Finally, isothermal sections calculated at  $T = 300, 700, 1200$ , and  $1700$  K are shown in Figs. 14a–d, respectively. The calculated equilibrium ternary phase fields should be confirmed experimentally to ascertain the predictions of our model. The isothermal section computed at  $T = 700$  K is in rather good agreement with that of Dash et al. [53], although the comparison is not straightforward. Dash et al. included  $\text{Ba}_3\text{MoO}_{24}$ ,  $\text{BaMo}_4\text{O}_{13}$ , and  $\text{Ba}_2\text{Mo}_5\text{O}_{17}$ , which were not taken into account in the present model due to the lack of structural and thermodynamic data (see Section 2). Nevertheless, the computed ternary phase fields are similar, except for  $\{\text{BaO}-\text{BaMoO}_3-\text{Ba}_3\text{MoO}_6\}$  calculated as a stable ternary phase field by Dash et al. [53], by contrast with the present work, showing instead an equilibrium between  $\{\text{Mo}-\text{BaO}-\text{Ba}_3\text{MoO}_6\}$  and  $\{\text{Mo}-\text{BaMoO}_3-\text{Ba}_2\text{MoO}_6\}$ .

## 7. Conclusions

The Ba-Mo-O system is rather complex, with a number of ternary barium molybdate phases reported in the literature. The thermodynamic modelling assessment for this system presented in this work includes  $\text{BaMoO}_4$ ,  $\text{Ba}_3\text{MoO}_6$ ,  $\text{Ba}_2\text{MoO}_5$ ,  $\text{BaMo}_2\text{O}_7$ ,  $\text{BaMo}_3\text{O}_{10}$ , and  $\text{BaMoO}_3$  solid phases, for which sufficient structural information is available. To provide experimental input for the optimization of the model using the CALPHAD method,  $\text{BaMoO}_4$ ,  $\text{BaMoO}_3$ , and  $\text{BaMo}_3\text{O}_{10}$  have been synthesized, and further used for thermodynamic property measurements. The valence state of molybdenum in the former two compounds was confirmed to be +VI and +IV, respectively, from XANES measurements at the Mo K-edge. Low-temperature heat capacity measurements on the same compositions have yielded  $S_m^o(\text{BaMoO}_4, \text{cr}, 298.15 \text{ K}) = (160.4 \pm 3.8) \text{ J} \cdot \text{K}^{-1} \cdot \text{mol}^{-1}$  and  $S_m^o(\text{BaMoO}_3, \text{cr}, 298.15 \text{ K}) = (111.3 \pm 2.8) \text{ J} \cdot \text{K}^{-1} \cdot \text{mol}^{-1}$ , respectively. Phase diagram measurements performed in the  $\text{BaMoO}_4-\text{MoO}_3$  section have revealed discrepancies with respect to earlier studies. Finally,  $\text{BaMo}_3\text{O}_{10}$  was suggested to undergo a peritectic decomposition and the transition enthalpy associated with this invariant reaction was determined as  $\Delta_{tr}H_m^o(\text{BaMo}_3\text{O}_{10}, \text{cr}, T_{tr}) = (82.8 \pm 20.0) \text{ kJ} \cdot \text{mol}^{-1}$ . The optimized thermodynamic model shows overall a good agreement with the literature and newly measured data. This study has highlighted, however, a number of poorly known properties and unresolved issues:

- the thermodynamic properties (enthalpy of formation, entropy, heat capacity, transition enthalpies) of  $\text{Ba}_3\text{MoO}_6$ ,  $\text{Ba}_2\text{MoO}_5$ ,  $\text{BaMo}_2\text{O}_7$ , and  $\text{BaMo}_3\text{O}_{10}$  have not been measured to this date;
- the existence of  $\text{BaMo}_2\text{O}_7$  should be ascertained and its crystal structure resolved;
- the phase equilibria between  $\text{BaMoO}_4$  and  $\text{MoO}_3$  are still poorly known and uncertain, with quite large discrepancies between past literature studies and this work. The vapour pressures in the ternary phase fields and above pure compounds were not discussed, and will be the subject of future studies.

## Declaration of Competing Interest

The authors report no declarations of interest.

<sup>6</sup> The stated uncertainty was derived based on the weighted average of the individual measurements.

## Acknowledgements

The experimental work was funded by the OECD/NEA TCOFF (Thermodynamic Characterisation of Fuel Debris and Fission Products Based on Scenario Analysis of Severe Accident Progression at Fukushima-Daiichi Nuclear Power Station) project. Modelling of the Ba-Mo-O system was supported by the OECD/NEA TAF-ID (Thermodynamics of Advanced Fuels – International Database) project. The authors would like to thank D. Banerjee (KU Leuven, Department of Chemistry) for his help with the XANES measurements at the BM26A-DUBBLE Beamline at the ESRF.

## Appendix A. Calorimetry data in the $\text{BaMoO}_4\text{-MoO}_3$ pseudo-binary section

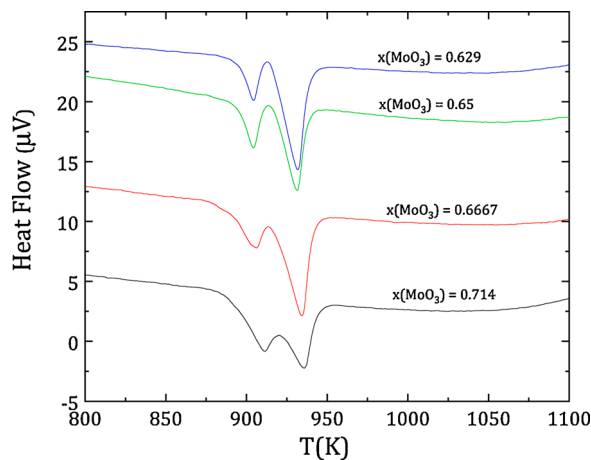


**Fig. A.1.** Heat flow curves measured in the  $\text{BaO}\text{-MoO}_3$  phase diagram.

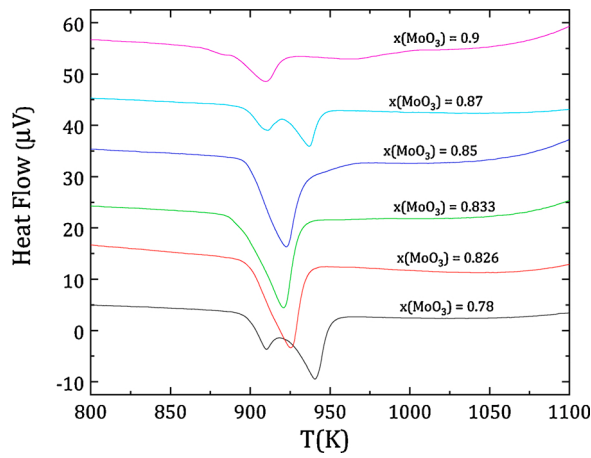


**Fig. A.2.** Heat flow curves measured in the  $\text{BaO}\text{-MoO}_3$  phase diagram.

## Appendix B. Thermodynamic modelling assessment of the Ba-O system

**Table B.1**

Summary of the thermodynamic data for pure elements and oxides selected in the Ba-O system. SER refers to the phase of the element stable at 298.15 K.

Phase	Gibbs energy/(J · mol <sup>-1</sup> )	Reference
Liquid (Ba <sup>2+</sup> )(O <sup>2-</sup> , Va <sup>Q-·O</sup> )	${}^0G(\text{Ba}^{2+})_2(O^{2-})_2 - 2{}^0H_{\text{Ba}}^{\text{SER}} - 2{}^0H_O^{\text{SER}} = 2G_{\text{Ba}}^{\text{Liq}} + 2G_O^{\text{Liq}} - 993855 + 100.235T$ ${}^0G(\text{Ba}^{2+})(\text{Va}^{Q-}) - {}^0H_{\text{Ba}}^{\text{SER}} = G_{\text{Ba}}^{\text{Liq}}$ ${}^0G(*)(O) - {}^0H_O^{\text{SER}} = G_O^{\text{SER}} - 2648.9 + 31.44T$ $L^0(\text{Ba}^{2+})_P(O^{2-}, \text{Va}^{Q-})_Q = -56504$	[26] [79] [79] [26]
Halite BaO (Ba <sup>2+</sup> , Va)(O <sup>2-</sup> , Va)	${}^0G(\text{Ba}^{2+})(O^{2-}) - {}^0H_{\text{Ba}}^{\text{SER}} - {}^0H_O^{\text{SER}} = G_{\text{BaO}}$ ${}^0G(\text{Ba}^{2+})(\text{Va}) - {}^0H_{\text{Ba}}^{\text{SER}} = G_{\text{Ba}}^{\text{SER}} + 100000$ ${}^0G(\text{Va})(O^{2-}) - {}^0H_O^{\text{SER}} = 0$ ${}^0G(\text{Va})(\text{Va}) = 0$	[26] [10] [10] [10]
BaO <sub>2</sub>	$G_{\text{BaO}_2} = -646278.5 + 370.156T - 69.91257T\ln(T)$ $-0.001927^2 + 3.2187 \cdot 10^{-7}T^3 + 213369.6T^{-1}(298 < T/K < 1142 \text{ K})$ $= -646118.4 + 379.243815T - 71.452T\ln(T)(1142 < T/K < 6000 \text{ K})$	[10] [10]
Ba (bcc) (Ba)(O, Va) <sub>3</sub>	${}^0G(\text{Ba})(\text{Va})_3 - {}^0H_{\text{Ba}}^{\text{SER}} = G_{\text{Ba}}^{\text{SER}}$ ${}^0G(\text{Ba})(\text{O})_3 - {}^0H_{\text{Ba}}^{\text{SER}} - 3{}^0H_O^{\text{SER}} = G_{\text{Ba}}^{\text{SER}} + 3G_O^{\text{SER}}$	[79] [10]
Gas (Ba,Ba <sub>2</sub> ,Ba <sub>2</sub> O <sub>2</sub> ,BaO,O,O <sub>2</sub> ,O <sub>3</sub> )	${}^0G_{\text{Ba}}^{\text{gas}} - {}^0H_{\text{Ba}}^{\text{SER}} = G_{\text{Ba}}^G + RT\ln(10^{-5}P)$ ${}^0G_{\text{Ba}_2}^{\text{gas}} - 2{}^0H_{\text{Ba}}^{\text{SER}} = G_{\text{Ba}_2}^G + RT\ln(10^{-5}P)$ ${}^0G_{\text{BaO}}^{\text{gas}} - {}^0H_{\text{Ba}}^{\text{SER}} = G_{\text{BaO}}^G + RT\ln(10^{-5}P)$ ${}^0G_{\text{Ba}_2\text{O}}^{\text{gas}} - 2{}^0H_{\text{Ba}}^{\text{SER}} - {}^0H_O^{\text{SER}} = G_{\text{Ba}_2\text{O}}^G + RT\ln(10^{-5}P)$ ${}^0G_{\text{Ba}_2\text{O}_2}^{\text{gas}} - 2{}^0H_{\text{Ba}}^{\text{SER}} - 2{}^0H_O^{\text{SER}} = G_{\text{Ba}_2\text{O}_2}^G + RT\ln(10^{-5}P)$ ${}^0G_O^{\text{gas}} - {}^0H_O^{\text{SER}} = G_O^G + RT\ln(10^{-5}P)$ ${}^0G_{\text{O}_2}^{\text{gas}} - 2{}^0H_O^{\text{SER}} = G_{\text{O}_2}^G + RT\ln(10^{-5}P)$ ${}^0G_{\text{O}_3}^{\text{gas}} - 3{}^0H_O^{\text{SER}} = G_{\text{O}_3}^G + RT\ln(10^{-5}P)$	[81] [81] [81] [81] [81] [81] [81] [81]
Functions	$G_O^{\text{SER}} = 1/2{}^0G_{\text{O}_2}^G$ $G_{\text{Ba}}^{\text{SER}} = -17685.226 + 233.78606T - 42.889T\ln(T) - 0.0018314T^2$ $-9.5 \cdot 10^{-11}T^3 + 705880T^{-1}(298 < T/K < 1000 \text{ K})$ $= -64873.614 + 608.188389T - 94.28241997T\ln(T) + 0.019504772T^2$ $-1.051353 \cdot 10^{-6}T^3 + 8220192T^{-1}(1000 < T/K < 2995 \text{ K})$ $G_{\text{Ba}}^{\text{Liq}} = -9738.988 + 229.540143T - 43.4961089T\ln(T) - 0.002346416T^2$ $+ 9.91223 \cdot 10^{-7}T^3 + 723016T^{-1}(298 < T/K < 1000 \text{ K})$ $= -7381.093 + 235.49642T - 45.1037T\ln(T) + 0.002154T^2$ $+ 2.7 \cdot 10^{-11}T^3 - 365T^{-1}(1000 < T/K < 2995 \text{ K})$ $= +11940.282 + 132.212T - 32.27T\ln(T)(2995 < T/K < 4000 \text{ K})$ $G_O^{\text{Liq}} = G_O^{\text{SER}} - 2648.9 + 31.44T(298 < T/K < 6000 \text{ K})$ $G_{\text{BaO}} = -562498.08 + 228.7677T - 43.5609T\ln(T) - 0.01114T^2$ $+ 2.3824667 \cdot 10^{-6}T^3 - 2.5271667 \cdot 10^{-10}T^4 + 88016.981T^{-1}(298 < T < 2280 \text{ K})$ $= -568509.864 + 310.40284T - 55.84644T\ln(T) + 2T^{-9}(2280 < T < 6000 \text{ K})$	[79] [79] [26]

**Table B.2**

Summary of the thermodynamic data for pure elements and oxides selected in the Ba-O system. SER refers to the phase of the element stable at 298.15 K.

Phase	Gibbs energy/(J·mol <sup>-1</sup> )	Reference
Ba	$G_{\text{Ba}}^G = +178685.405 - 28.7519079T - 21.15208T\ln(T)$ $+ 4.6163325 \cdot 10^{-4}T^2 - 1.00440133 \cdot 10^{-7}T^3 + 6531.67T^{-1}$ $(298 < T < 1000 \text{ K})$ $= +156541.305 + 187.123918T - 52.09573T\ln(T)$ $+ 0.019772705T^2 - 2.37413833 \cdot 10^{-6}T^3 + 2988594.5T^{-1}$ $(1000 < T < 1900 \text{ K})$ $= +444158.608 - 1453.56939T + 163.8061T\ln(T)$ $- 0.05237755T^2 + 2.155975 \cdot 10^{-6}T^3 - 68947450T^{-1}$ $(1900 < T < 2600 \text{ K})$ $= +354853.605 - 1163.84325T + 129.0623T\ln(T) - 0.047641765T^2$ $+ 2.12269167 \cdot 10^{-6}T^3 - 30187880T^{-1}$ $(2600 < T < 3400 \text{ K})$ $= -502647.818 + 193.17624T - 252.1979T\ln(T) + 0.027795155T^2$ $- 6.79449667 \cdot 10^{-7}T^3 + 3.319067 \cdot 10^8T^{-1}$ $(3400 < T < 5300 \text{ K})$ $= +229718.753 + 82.4114527T - 35.204357T\ln(T) - 8.066315 \cdot 10^{-4}T^2$ $+ 2.79384333 \cdot 10^{-8}T^3 - 1.3210115 \cdot 10^8T^{-1}$ $(5300 < T < 9600 \text{ K})$ $G_{\text{Ba}_2}^G = +343727.221 + 33.4913106T - 51.13698T\ln(T)$ $+ 0.03220523T^2 - 6.47438 \cdot 10^{-6}T^3 - 72907.6T^{-1}$ $(298 < T < 600 \text{ K})$ $= +356118.559 - 158.369248T - 21.31458T\ln(T) + 2.0490545 \cdot 10^{-4}T^2$ $- 1.36280533 \cdot 10^{-8}T^3 - 1040998.5T^{-1}$ $(600 < T < 3000 \text{ K})$ $G_{\text{BaO}}^G = -129260.91 - 2.02743809T - 34.4359T\ln(T)$ $- 0.0024537165T^2 + 3.34474 \cdot 10^{-7}T^3 + 126036.5T^{-1}$ $(298 < T < 1100 \text{ K})$ $= -138831.073 + 79.8873471T - 45.95129T\ln(T) + 0.003913731T^2$	[81]
Ba <sub>2</sub> O		[81]
		[81]

*(continued on next page)*

**Table B.2 (continued)**

Phase	Gibbs energy/(J·mol <sup>-1</sup> )	Reference
	$-3.55722167 \cdot 10^{-7}T^3 + 1649835T^{-1}$ (1100 < T < 2400 K) $= -111463.793 + 19.5306837T - 39.56298T\ln(T) + 0.00507084T^2$ $-5.66334 \cdot 10^{-7}T^3 - 11782225T^{-1}$ (2400 < T < 3800 K) $= +597280.146 - 2356.2218T + 249.8813T\ln(T) - 0.04754315T^2$ $+1.229221 \cdot 10^{-6}T^3 - 3.377278 \cdot 10^8T^{-1}$ (3800 < T < 5900 K) $G_{Ba_2O}^G = -259922.912 + 87.0305009T - 55.15417T\ln(T)$ $-0.00662439T^2 + 1.14898217 \cdot 10^{-6}T^3 + 290806.05T^{-1}$ (298 < T < 900 K) $= -263453.85 + 134.319936T - 62.3304T\ln(T) - 4.2961955 \cdot 10^{-6}T^2$ $+5.301555 \cdot 10^{-11}T^3 + 632566.5T^{-1}$ (900 < T < 3000 K) $G_{Ba_2O_2}^G = -527525.33 + 137.41572T - 73.014T\ln(T)$ $-0.006415T^2 + 1.0547333 \cdot 10^{-6}T^3 + 244760T^{-1}$ (298 < T < 1000 K) $= -542321.87 + 277.3629T - 92.986T\ln(T)$ $+0.00606751^2 - 6.0775 \cdot 10^{-7}T^3 + 2235800T^{-1}$ (1000 < T < 2200 K) $= -624554.56 + 801.39277T - 162.89T\ln(T) + 0.03152T^2 - 2.3005 \cdot 10^{-6}T^3 + 19379500T^{-1}$ (2200 < T < 3600 K)	[81]

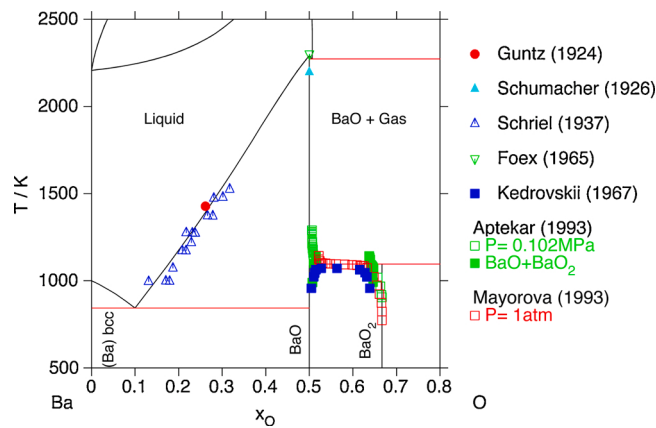


**Fig. B.1.** Ba-O phase diagram computed at 1 bar, and comparison with the experimental data of Guntz and Benoit [100], Schumacher [101], Schriehl [102], Foex [103], Kedrovskii et al. [104], Aptekar et al. [27], Mayorova et al. [28].

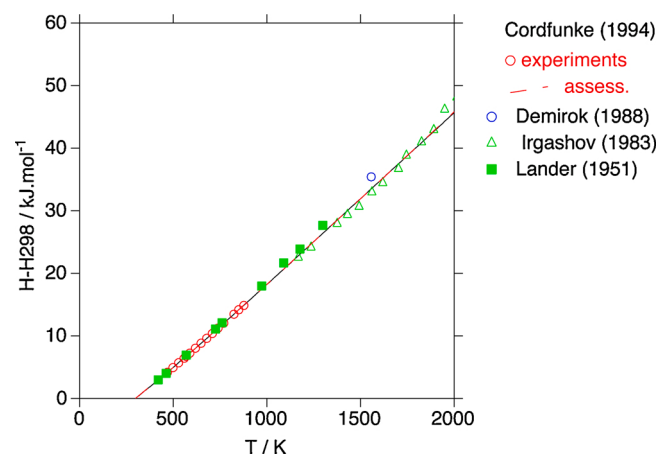


**Fig. B.3.** Enthalpy increment of BaO computed at 1 bar, and comparison with the experimental data of Cordfunke [105], Demirok [110], Irgashov [111] and Lander [112].

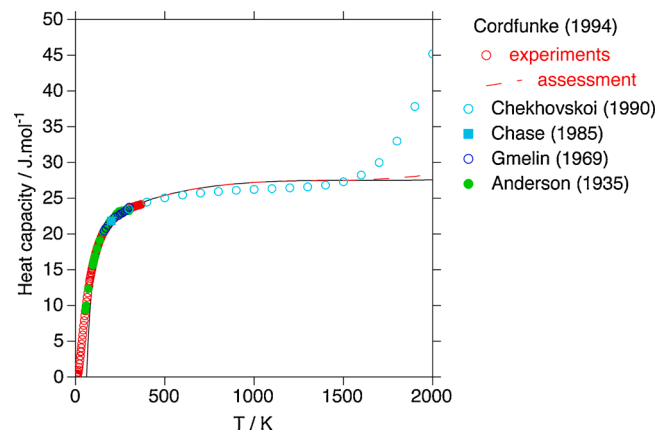


**Fig. B.2.** Heat capacity of BaO computed at 1 bar, and comparison with the experimental data of Cordfunke [105], Chekhovskoi [106], NIST-JANAF [107], Gmelin [108], and Anderson [109].

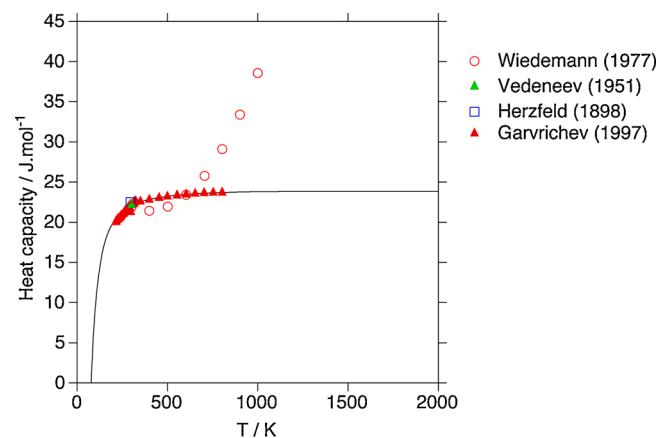


**Fig. B.4.** Heat capacity of BaO<sub>2</sub> computed at 1 bar, and comparison with the experimental data of Wiedemann [113], Vedeneev [114], Herzfeld and Stiepel [115], and Gavrichev et al. [116].

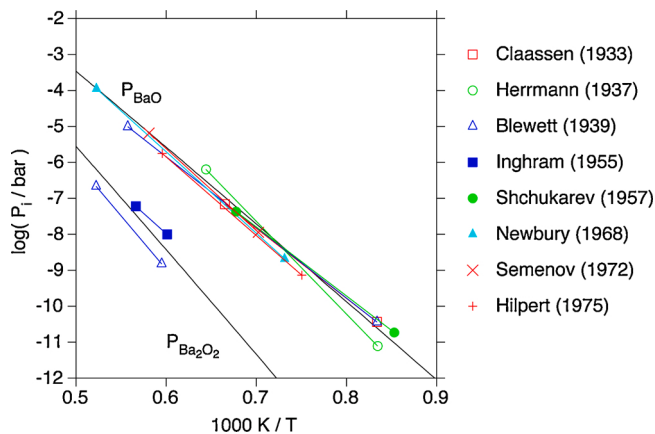


**Fig. B.5.** Computed partial pressures over BaO, and comparison with the experimental data of Claassen and Veenemans [117], Herrmann [118], Blewett et al. [119], Inghram et al. [120], Shchukarev and Semenov [121], Newbury et al. [122], Semenov et al. [123], Hilpert and Gerads [124].

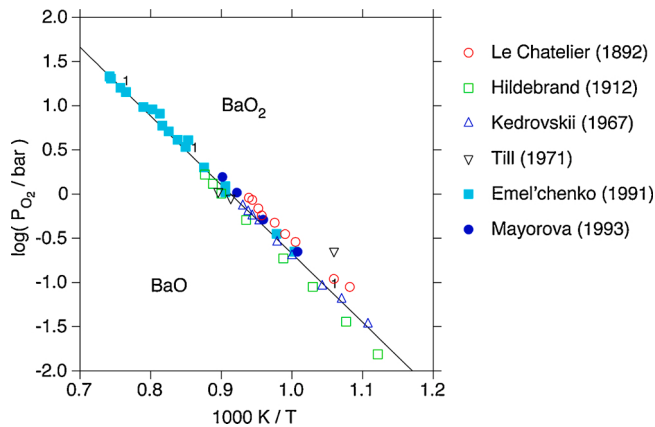


**Fig. B.6.** Computed oxygen partial pressure over {BaO+BaO<sub>2</sub>}, and comparison with the experimental data of Le Chatelier [125], Hildebrand [126], Kedrovskii et al. [104], Till [127], Emel'chenko et al. [128], and Mayorova et al. [28].

### Appendix C. Thermodynamic modelling assessment of the Ba-Mo system

**Table C.1**

Summary of the thermodynamic data for pure elements and oxides selected in the Ba-Mo system. SER refers to the phase of the element stable at 298.15 K.

Phase	Gibbs energy/(J · mol <sup>-1</sup> )	Reference
Liquid (Ba <sup>2+</sup> ,Mo <sup>4+</sup> )(Va <sup>Q-</sup> )	${}^{\circ}\text{G}(\text{Ba}^{2+})(\text{Va}^{Q-}) - {}^{\circ}\text{H}_{\text{Ba}}^{\text{SER}} = \text{G}_{\text{Ba}}^{\text{Liq}}$ ${}^{\circ}\text{G}(\text{Mo}^{4+})(\text{Va}^{Q-}) - {}^{\circ}\text{H}_{\text{Mo}}^{\text{SER}} = \text{G}_{\text{Mo}}^{\text{Liq}}$ $\text{L}^0(\text{Ba}^{2+},\text{Mo}^{4+})_p(\text{Va}^{Q-})_Q = +100000$ $\text{L}^1(\text{Ba}^{2+},\text{Mo}^{4+})_p(\text{Va}^{Q-})_Q = -50000$	[79] [79] [10] [10]
(Ba,Mo) (bcc) (Ba,Mo)(Va) <sub>3</sub>	${}^{\circ}\text{G}(\text{Ba})(\text{Va})_3 - {}^{\circ}\text{H}_{\text{Ba}}^{\text{SER}} = \text{G}_{\text{Ba}}^{\text{SER}}$ ${}^{\circ}\text{G}(\text{Mo})(\text{Va})_3 - {}^{\circ}\text{H}_{\text{Mo}}^{\text{SER}} = \text{G}_{\text{Mo}}^{\text{SER}}$ $\text{L}^0(\text{Ba,Mo})(\text{Va})_3 = +100000$ $\text{L}^1(\text{Ba,Mo})(\text{Va})_3 = -50000$	[79] [79] [10] [10]
Gas (Ba,Ba <sub>2</sub> ,Mo,Mo <sub>2</sub> )	${}^{\circ}\text{G}_{\text{Ba}}^{\text{gas}} - {}^{\circ}\text{H}_{\text{Ba}}^{\text{SER}} = \text{G}_{\text{Ba}}^{\text{G}}$ + RT ln(10 <sup>-5</sup> P) ${}^{\circ}\text{G}_{\text{Ba}_2}^{\text{gas}} - 2{}^{\circ}\text{H}_{\text{Ba}}^{\text{SER}} = \text{G}_{\text{Ba}_2}^{\text{G}}$ + RT ln(10 <sup>-5</sup> P) ${}^{\circ}\text{G}_{\text{Mo}}^{\text{gas}} - {}^{\circ}\text{H}_{\text{Mo}}^{\text{SER}} = \text{G}_{\text{Mo}}^{\text{G}}$ + RT ln(10 <sup>-5</sup> P) ${}^{\circ}\text{G}_{\text{Mo}_2}^{\text{gas}} - 2{}^{\circ}\text{H}_{\text{Mo}}^{\text{SER}} = \text{G}_{\text{Mo}_2}^{\text{G}}$ + RT ln(10 <sup>-5</sup> P)	[81] [81] [79] [79]

(continued on next page)

**Table C.1 (continued)**

Phase	Gibbs energy/(J · mol <sup>-1</sup> )	Reference
Functions	$G_{\text{Ba}}^{\text{SER}} = -17685.226 + 233.78606T - 42.889T\ln(T) - 0.0018314T^2 - 9.5 \cdot 10^{-11}T^3 + 705880T^{-1}$ (298 < T/K < 1000 K) $= -64873.614 + 608.188389T - 94.2824199T\ln(T) + 0.019504772T^2 - 1.051353 \cdot 10^{-6}T^3 + 8220192T^{-1}$ (1000 < T/K < 2995 K) $G_{\text{Mo}}^{\text{SER}} = -7746.302 + 131.9197T - 23.56414T\ln(T) - 0.003443396T^2 + 5.66283 \cdot 10^{-7}T^3 + 65812T^{-1} - 1.30927 \cdot 10^{-10}T^4$ (298 < T/K < 2896 K) $G_{\text{Ba}}^{\text{Liq}} = -9738.988 + 229.540143T - 43.4961089T\ln(T) - 0.002346416T^2 + 9.91223 \cdot 10^{-7}T^3 + 723016T^{-1}$ (298 < T/K < 1000 K) $= -7381.093 + 235.49642T - 45.103T\ln(T) + 0.002154T^2 + 2.7 \cdot 10^{-11}T^3 - 365T^{-1}$ (1000 < T/K < 2995 K) $= +11940.282 + 132.212T - 32.2T\ln(T)$ (2995 < T/K < 4000 K) $G_{\text{Mo}}^{\text{Liq}} = +34085.045 + 117.224788T - 23.56414T\ln(T) - 0.003443396T^2 + 5.66283 \cdot 10^{-7}T^3 + 65812T^{-1} - 1.30927 \cdot 10^{-10}T^4 + 4.24519 \cdot 10^{-22}T^7$ (298 < T < 2896 K) $= +3538.963 + 271.6697T - 42.63829T\ln(T)$ (2896 < T < 5000 K)	[79]
		[79]
		[79]
		[79]
		[79]

**Table C.2**

Summary of the thermodynamic data for pure elements and oxides selected in the Ba-Mo system. SER refers to the phase of the element stable at 298.15 K.

Phase	Gibbs energy/(J · mol <sup>-1</sup> )	Reference
$G_{\text{Ba}}^G = +178685.405 - 28.7519079T - 21.15208T\ln(T) + 4.6163325 \cdot 10^{-4}T^2 - 1.00440133 \cdot 10^{-7}T^3 + 6531.67T^{-1}$	(298 < T < 1000 K)	[81]
$= +156541.305 + 187.123918T - 52.09573T\ln(T) + 0.019772705T^2 - 2.37413833 \cdot 10^{-6}T^3 + 2988594.5T^{-1}$	(1000 < T < 1900 K)	
$= +444158.608 - 1453.56939T + 163.8061T\ln(T) - 0.05237755T^2 + 2.155975 \cdot 10^{-6}T^3 - 68947450T^{-1}$	(1900 < T < 2600 K)	
$= +354853.605 - 1163.84325T + 129.0623T\ln(T) - 0.047641765T^2 + 2.12269167 \cdot 10^{-6}T^3 - 30187880T^{-1}$	(2600 < T < 3400 K)	
$= -502647.818 + 1933.17624T - 252.1979T\ln(T) + 0.027795155T^2 - 6.79449667 \cdot 10^{-7}T^3 + 3.319067 \cdot 10^8T^{-1}$	(3400 < T < 5300 K)	
$= +229718.753 + 82.4114527T - 35.20435T\ln(T) - 8.066315 \cdot 10^{-4}T^2 + 2.79384333 \cdot 10^{-8}T^3 - 1.3210115 \cdot 10^8T^{-1}$	(5300 < T < 9600 K)	
$G_{\text{Ba}_2}^G = +343727.221 + 33.4913106T - 51.13698T\ln(T) + 0.03220523T^2 - 6.47438 \cdot 10^{-6}T^3 - 72907.6T^{-1}$	(298 < T < 600 K)	[81]
$= +356118.559 - 158.369248T - 21.31458T\ln(T) + 2.0490545 \cdot 10^{-4}T^2 - 1.36280533 \cdot 10^{-8}T^3 - 1040998.5T^{-1}$	(600 < T < 3000 K)	
$G_{\text{Mo}}^G = +651326.983 - 41.0946081T - 21.0437T\ln(T) + 2.7252545 \cdot 10^{-4}T^2 - 4.77857833 \cdot 10^{-8}T^3 + 5594.93T^{-1}$	(298 < T < 1600 K)	[81]
$= +633752.125 + 83.3186552T - 37.98605T\ln(T) + 0.007623775T^2 - 6.52545667 \cdot 10^{-7}T^3 + 3471277.5T^{-1}$	(1600 < T < 3500 K)	
$= +1134689.66 - 1617.69443T + 169.66587T\ln(T) - 0.03080567T^2 + 6.87557667 \cdot 10^{-7}T^3 - 2.240338 \cdot 10^8T^{-1}$	(3500 < T < 5000 K)	
$= +1008188.16 - 1437.30781T + 150.73957T\ln(T) - 0.03086233T^2 + 7.54569333 \cdot 10^{-7}T^3 - 1.0601775 \cdot 10^8T^{-1}$	(5000 < T < 6200 K)	
$G_{\text{Mo}_2}^G = +892320.138 + 5.95304372T - 37.156T\ln(T) + 3.61 \cdot 10^{-5}T^2 - 1.10858333 \cdot 10^{-7}T^3 + 113615T^{-1}$	(298 < T < 1000 K)	[81]
$= +878307.025 + 162.383892T - 60.077T\ln(T) + 0.0165846T^2 - 2.3378 \cdot 10^{-6}T^3 + 1706980T^{-1}$	(1000 < T < 1800 K)	
$= +1105100.83 - 1223.34666T + 124.219T\ln(T) - 0.05020415T^2 + 2.21706167 \cdot 10^{-6}T^3 - 50788800T^{-1}$	(1800 < T < 3100 K)	
$= +641365.422 + 619.744903T - 105.798T\ln(T) + 6.5385 \cdot 10^{-4}T^2 + 1.02916667 \cdot 10^{-7}T^3 + 1.25079 \cdot 10^8T^{-1}$	(3100 < T < 6000 K)	

**Appendix D. Supplementary data**Supplementary data associated with this article can be found, in the online version, at <https://doi.org/10.1016/j.jeurceramsoc.2021.01.010>.**References**

- [1] G. Brillant, J. Nucl. Mater. 397 (2010) 40–47.
- [2] M. Barrachin, D. Gavillet, R. Dubourg, A. De Bremaecker, J. Nucl. Mater. 453 (2014) 340–354.
- [3] Thermodynamic Characterization of Fuel Debris and Fission Products Based on Scenario Analysis of Severe Accident Progression at Fukushima-Daiichi Nuclear Power Station (TCOFF), 2020., OECD, NEA, Technical Report, www.oecd-nea.org/science/tcoff/.
- [4] H. Kleykamp, J. Nucl. Mater. 131 (1985) 221–246.
- [5] S. Imoto, J. Nucl. Mater. 140 (1986) 19–27.
- [6] E.H.P. Cordfunke, R.J.M. Konings, J. Nucl. Mater. 152 (1988) 301–309.
- [7] E.H.P. Cordfunke, R.J.M. Konings, J. Nucl. Mater. 201 (1993) 57–69.
- [8] K. Kurosaki, K. Tanaka, M. Osaka, Y. Ohishi, H. Muta, M. Uno, S. Yamanaoka, Prog. Nucl. Sci. Technol. 2 (2011) 5–8.
- [9] T. Miromura, T. Adachi, H. Takeishi, Z. Yoshida, T. Yamamoto, K. Ueno, J. Nucl. Mater. 151 (1988) 318–326.
- [10] Thermodynamics of Advanced Fuels-International Database (TAF-ID), 2020., OECD, NEA, Technical report, www.oecd-nea.org/science/taf-id/.
- [11] J.-W. Yoon, J.H. Ryu, K.B. Shim, Mater. Sci. Eng. B 127 (2006) 154–158.
- [12] L.S. Cavalcante, J.C. Szczanski, R.L. Tranquillini, M.R. Joya, P.S. Pizani, J. A. Varela, E. Longo, J. Phys. Chem. Solids 69 (11) (2008) 2674–2680.
- [13] M. Lei, C.X. Ye, S.S. Ding, K. Bi, H. Xiao, Z.B. Sun, D.Y. Fan, H.J. Yang, Y.G. Wang, J. Alloys Compd. 639 (2015) 102–105.
- [14] A. Kato, S. Oishi, T. Shishido, M. Yamazaki, S. Iida, J. Phys. Chem. Solids 66 (2005) 2079–2081.
- [15] E.V. Zharkov, C. Zaldo, F. Diaz, Recent advances in bulk crystal growth, MRS Bull. 34 (4) (2009) 271–276.

- [16] J. Bi, L. Wu, Y. Zhang, Z. Li, J. Li, X. Fu, *Appl. Catal. B: Environ.* 91 (1–2) (2009) 135–143.
- [17] H.H. Li, K.W. Li, H. Wang, *Mater. Chem. Phys.* 116 (2009) 134–142.
- [18] Y.-J. Chen, X.-M. Gao, X.-P. Di, Q.-Y. Ouyang, P. Gao, L.-H. Qi, C.-Y. Li, C.-L. Zhu, *ACS Appl. Mater. Interfaces* 5 (2013) 3267–3274.
- [19] G.-K. Choi, S.-Y. Cho, J.-S. An, K.S. Hong, *J. Eur. Ceram. Soc.* 26 (2006) 2011–2015.
- [20] H. Kähäri, M. Teirikangas, J. Juuti, H. Jantunen, *J. Am. Ceram. Soc.* 97 (2014) 3378–3379.
- [21] K. Kuroaki, T. Oyama, H. Muta, M. Uno, S. Yamanaka, *J. Alloys Compd.* 372 (2004) 65–69.
- [22] C. Shrivakumar, R. Saraf, S. Behera, N. Dhananjaya, H. Nagabhushana, *Spectrochim. Acta Part A: Mol. Biomol. Spectrosc.* 151 (2015) 141–148.
- [23] C. Guéneau, S. Gosse, A. Quani, N. Dupin, B. Sundman, M. Kurata, T. Besmann, P. Turchi, J.-C. Dumas, E.-C. Corcoran, et al., Range of DLS comes around FUELBASE, TAF-ID databases and OC software. Advanced computational tools to perform thermodynamic calculations on nuclear fuel materials, in: The 7th European Review Meeting on Severe Accident Research (ERMSAR-2015), Marseille, France, 24–26 March 2015, 2015. Technical Report.
- [24] T.B. Massalski, volume 1. 2nd edition, (1990).
- [25] E. Zimmermann, K. Hack, D. Neuschütz, *Calphad* 19 (1985) 119–127.
- [26] S. Zhou, R. Arroyave, C.A. Randall, Z.-K. Liu, *J. Am. Ceram. Soc.* 88 (7) (2005) 1943–1948.
- [27] I.L. Aptekar, G.A. Emel'chenko, A.V. Kosenko, *Solid State Commun.* 87 (1993) 227–231.
- [28] A.F. Maurova, S.N. Mudretsova, M.N. Mamontov, P.A. Levashov, A.D. Rusin, *Thermochim. Acta* 217 (1993) 241–249.
- [29] E.C. Corcoran, J.-L. Flèche, N. Dupin, B. Sundman, C. Guéneau, *Calphad* 63 (2018) 196–211.
- [30] G. Kauric, Etude de l'interaction entre le Combustible MOX et le Sodium Pour la Sureté des Réacteurs à Neutrons Rapides à Caloporteur Sodium (RNR), Study of the Nuclear Fuel-Sodium Coolant Interaction for the Safety Assessment of Sodium-Cooled Fast Reactors. PhD Thesis, University Paris-Saclay, France, 2020.
- [31] F.A. Rabuffetti, S.P. Culver, L. Suescun, R.L. Brutchey, *Inorg. Chem.* 53 (2014) 1056–1061.
- [32] N.N. Shevchenko, L.N. Lykova, L.M. Kovba, *Russ. J. Inorg. Chem.* 19 (1974) 528–530.
- [33] R. Sabatier, M. Wathle, J.P. Besse, G. Baud, C.R. Seances Acad. Sci. Ser. C 271 (1970) 368–371.
- [34] P.E. Werner, M. Moustakimov, B.O. Marinder, K.S. Knight, *Z. Kristallogr.* 212 (1997) 665–670.
- [35] H.A. Hopper, J. Le, J. Cheng, T.M. Weller, R. Marschall, J.Z. Bloh, D.E. Macphee, A. Folli, A.C. McLaughlin, *J. Solid State Chem.* 234 (2016) 87–92.
- [36] N. Barrier, P. Gougeon, R. Retoux, *J. Alloys Compd.* 317/318 (2001) 120–126.
- [37] K.H. Lii, C.C. Wang, S.L. Wang, *J. Solid State Chem.* 77 (1988) 407–411.
- [38] G.L. Schimek, D.A. Nagaki, R.E. McCarley, *Inorg. Chem.* 33 (1994) 1259–1265.
- [39] C.C. Torardi, R.E. McCarley, *J. Less-Common Metals* 116 (1986) 169–186.
- [40] G. Tammann, F. Westerhold, Z. Anorg. Allg. Chem. 149 (1925) 25.
- [41] V.L. Lavrent'ev, Ya.I. Gerasimov, T.N. Rezukhina, *Nauk. SSSR Dokl. Akad.* 133 (1960) 374.
- [42] E.H.P. Cordfunke, R.J.M. Konings, Thermochemical Data for Reactor Materials and Fission Products, Elsevier Science Publishers B.V., 1990.
- [43] T. N. Rezukhina, PhD thesis, University of Moscow, (1968).
- [44] P.A.G. O'Hare, *J. Chem. Thermodyn.* 6 (1974) 425.
- [45] N.K. Shukla, R. Prasad, D.D. Sood, *J. Chem. Thermodyn.* 25 (1993) 429–434.
- [46] Z. Singh, S. Dash, R. Prasad, V. Venugopal, *J. Alloys Compd.* 266 (1998) 77–80.
- [47] O. Kubaschewski, *High Temp. High Press.* 4 (1972).
- [48] R. Guillaumont, T. Fanghänel, J. Fuger, I. Grenthe, V. Neck, D.A. Palmer, M. H. Rand, Update on the Chemical Thermodynamics of Uranium, Neptunium, Plutonium, Americium & Technetium, OECD Nuclear Energy Agency, Data Bank, 2003.
- [49] M. Morishita, M. Fukushima, H. Houshiyama, *Mater. Trans.* 57 (2016) 46–51.
- [50] R. Saha, R. Babu, K. Nagarajan, C.K. Mathews, *Thermochim. Acta* 120 (1987) 29–39.
- [51] Z. Singh, S. Dash, R. Prasad, V. Venugopal, *J. Alloys Compd.* 279 (1998) 287–294.
- [52] M. Sahu, K. Krishnan, B.K. Nagar, D. Jain, M.K. Saxena, C.G.S. Pillai, S. Dash, *J. Nucl. Mater.* 427 (2012) 323–332.
- [53] S. Dash, Z. Singh, R. Prasad, V. Venugopal, *High Temp. Press.* 32 (2000) 215–225.
- [54] D.L. Perry, Taylor & Francis Group, second edition, (2011).
- [55] O. Knacke, O. Kubaschewski, and K. Hesselmann. Springer-Verlag, (1991).
- [56] O.A. Ustinov, G.P. Novoselov, M.A. Andrianov, N.T. Chebotarev, *Russ. J. Inorg. Chem.* 15 (9) (1970) 1320–1321.
- [57] A.E. Musikhin, V.N. Naumov, M.V. Chislov, I.A. Zvereva, *Thermochim. Acta* 661 (2018) 160–165.
- [58] W.W. Ge, H.J. Zhang, J.Y. Wang, J.H. Liu, X.G. Xu, X.B. Hu, M.H. Jiang, D.G. Ran, S.Q. Sun, H.R. Xia, *J. Appl. Phys.* 98 (2005) 013542.
- [59] T.N. Rezukhina, V.A. Levitskii, *Izv. Akad. Nauk. SSSR. Neorg. Mater.* 3 (1967) 138.
- [60] L.A. Zharkova, N.G. Baraneeva, *Zh. Fiz. Khim.* 38 (1964) 752.
- [61] S. Dash, Z. Singh, R. Prasad, D.D. Sood, *J. Nucl. Mater.* 207 (1993) 350–352.
- [62] H. Yokokawa, N. Sakai, T. Kawada, M. Dokiya, *J. Solid State Chem.* 94 (1991) 106–120.
- [63] R. Agarwal, Z. Singh, V. Venugopal, *J. Alloys Compd.* 282 (1999) 231–235.
- [64] S. Yamanaka, K. Kuroaki, T. Maekawa, T. Matsuda, S. Kobayashi, M. Uno, *J. Nucl. Mater.* 344 (2005) 61–66.
- [65] M. Sahu, K. Krishnan, M.K. Saxena, S. Dash, *J. Nucl. Mater.* 457 (2015) 29–35.
- [66] J.O.A. Paschoal, H. Kleykamp, F. Thummel, *J. Nucl. Mater.* 151 (1987) 10–21.
- [67] Z. Singh, S. Dash, R. Prasad, V. Venugopal, *J. Solid State Chem.* 134 (1997) 416–419.
- [68] T.M. Yanushkevich, V.M. Zhukovskii, *Inorg. Mater. (Engl. Transl.)* 8 (1972) 1794–1795.
- [69] V.M. Zhukovskii, E.V. Tkachenko, T.A. Rakova, *Russ. J. Inorg. Chem.* 15 (12) (1970) 1734–1736.
- [70] T.M. Besmann, Chemical Technology Division, Oak Ridge National Laboratory, Oak Ridge, 37830 TN, USA, Technical Report ORNL-TM-5775, (1977).
- [71] J. Rodriguez-Carvajal, *Physica B* 192 (1993) 55–69.
- [72] B. Ravel, M. Newville, *J. Synchrotron Radiat.* 12 (2005) 537–541.
- [73] J.C. Lashley, M.F. Hundley, A. Migliori, J.L. Sarrao, P.G. Pagliuso, T.W. Darling, M. Jaime, J.C. Cooley, W.L. Hults, L. Morales, D.J. Thoma, J.L. Smith, J. Boerio-Goates, B.F. Woodfield, G.R. Stewart, R.A. Fisher, N.E. Phillips, *Cryogenics* 43 (6) (2003) 369–378.
- [74] P. Javoryš, F. Wastin, E. Colineau, J. Rebizant, P. Boulet, G. Stewart, *J. Nucl. Mater.* 344 (2005) 50–55.
- [75] G.W.H. Höhne, H.K. Cammenga, W. Eysel, E. Gmelin, W. Hemminger, *Thermochim. Acta* 160 (1990) 1–12.
- [76] G.D. Gatta, M.J. Richardson, S.M. Sarge, S. Stolen, *Pure Appl. Chem.* 78 (7) (2006) 1455–1476.
- [77] Jansson B., Technical report, (1984).
- [78] B. Sundman, B. Jansson, J.O. Andersson, *Calphad* 9 (1985) 153–190.
- [79] A. Dinsdale, *Calphad* 15 (1991) 317–425.
- [80] M. Hillert, B. Jansson, B. Sundman, J. Agren, *Metall. Trans. A* 16 (1) (1985) 261–266.
- [81] I. Ansara, B. Sundman, Scientific Group Thermodata Europe, Computer Handling and Determination of Data, North Holland, Amsterdam, 1986.
- [82] F. Rocca, A. Kuzmin, P. Mustarelli, C. Tomasi, A. Magistris, *Solid State Ionics* 121 (1999) 189–192.
- [83] A. Kuzmin, J. Purans, *J. Phys.: Condens. Matter* 12 (2000) 1959–1970.
- [84] H. Aritani, T. Tanaka, T. Funabiki, S. Yoshida, M. Kudo, S. Hasegawa, *J. Phys. Chem.* 100 (1996) 5440–5446.
- [85] J. Majzlan, A. Navrotsky, B.F. Woodfield, B.E. Lang, J. Boerio-Goates, R.A. Fisher, *J. Low Temp. Phys.* 130 (1–2) (2003) 69–76.
- [86] E.S. Gopal, Specific Heats at Low Temperatures, Plenum Press, 1966.
- [87] S. Hayashi, Aoki, *Mat. Res. Bull.* 14 (1979) 409–413.
- [88] P.F. Rosen, B.F. Woodfield, *J. Chem. Thermodyn.* 141 (2020) 105974.
- [89] Q. Shi, L. Zhang, M.E. Schlesinger, J. Boerio-Goates, B.F. Woodfield, *J. Chem. Thermodyn.* 61 (2013) 51–57.
- [90] Q. Shi, L. Zhang, M.E. Schlesinger, J. Boerio-Goates, B.F. Woodfield, *J. Chem. Thermodyn.* 62 (2013) 35–42.
- [91] Q. Shi, L. Zhang, M.E. Schlesinger, J. Boerio-Goates, B.F. Woodfield, *J. Chem. Thermodyn.* 62 (2013) 35–42.
- [92] B.F. Woodfield, J. Boerio-Goates, J.L. Shapiro, R.L. Putnam, A. Navrotsky, *J. Chem. Thermodyn.* 31 (1999) 245–253.
- [93] B.F. Woodfield, J.L. Shapiro, R. Stevens, J. Boerio-Goates, R.L. Putnam, K. B. Helean, A. Navrotsky, *J. Chem. Thermodyn.* 31 (1999) 1573–1583.
- [94] A.L. Smith, G. Kauric, L. van Eijck, K. Goubitz, G. Wallez, J.-C. Griveau, E. Colineau, N. Clavier, R.J.M. Konings, *J. Solid State Chem.* 253 (2017) 89–102.
- [95] A.L. Smith, M.-C. Pignié, L. van Eijck, J.-C. Griveau, E. Colineau, R.J.M. Konings, *J. Chem. Thermodyn.* 120 (2018) 205–216.
- [96] A.L. Smith, N. de Zoete, M. Rutten, L. van Eijck, J.-C. Griveau, E. Colineau, *Inorg. Chem.* 59 (18) (2020) 13162–13173.
- [97] A.L. Smith, J.-C. Griveau, E. Colineau, P.E. Raison, G. Wallez, R.J.M. Konings, *J. Chem. Thermodyn.* 91 (2015) 245–255.
- [98] A.L. Smith, E. Colineau, J.-C. Griveau, K. Popa, G. Kauric, P. Martin, A. C. Scheinost, A.K. Cheetham, R.J.M. Konings, *Inorg. Chem.* 56 (2017) 5839–5850.
- [99] E. Epifano, G. Wallez, A. Volfi, M. Abbink, H. Nieuwland, D. Banerjee, P. M. Martin, A.L. Smith, *Inorg. Chem.* (2020).
- [100] M.A. Gunzt, F. Benoit, *Bull. Soc. Chim.* 35 (1924) 709.
- [101] E.E. Schumacher, *J. Am. Chem. Soc.* 48 (1926) 396.
- [102] M. Schriek, Z. anorg. Allg. Chem. 231 (1937) 313.
- [103] M. Foex, *Sol. Energy* 9 (1965) 61.
- [104] O.V. Kedrovskii, P.V. Kovtunenko, E.V. Kiseleva, A.A. Bundel, *Russ. J. Phys. Chem.* 41 (1967) 205–208.
- [105] E.H.P. Cordfunke, R.R. van der Laan, J. van, Miltensburg, *J. Phys. Chem. Solids* 55 (1994) 77–84.
- [106] V.Ya. Chekhovskoi, V.D. Tarasov, *Zh. Fiz. Khim.* 64 (1990) 2.
- [107] M. Schriek, Z. anorg. Allg. Chem. 231 (1937) 313.
- [108] E. Gmelin, *Naturforsch* 24A (1969) 1794.
- [109] C.T. Anderson, *J. Am. Soc.* 57 (1935) 429.
- [110] S. Demirok, Diplomarbeit, RWTH Aachen, 1988. Technical Report.
- [111] K. Irgashov, V.D. Tarasov, V.Y. Chekhovskoi, *Teplofizika Vysokikh Temp.* 21 (1983) 900.
- [112] J.J. Lander, *J. Am. Chem. Soc.* 73 (1951) 5794.
- [113] H.-G. Wiedemann, G. Bayer, *Chemtech* 7 (1977) 381.
- [114] A.V. Vedeneev, S.M. Skuratov, *Zhur. Fiz. Khim.* 25 (1951) 837.
- [115] A. Herzfeld and K. Stiepel, *Z. Ver. f. Rübenzuckerindustrie* (1898) 84.
- [116] K.S. Garvichev, V.E. Gorbunov, M.V. Gorbatcheva, A.F. Maiorova, S. N. Mudretsova, Y.Y. Skol'skii, M.L. Kovba, *Zh. Neorg. Khim.* 42 (1997) 1158–1162.
- [117] A. Claassen, C.F. Veenemans, *Z. Phys.* 80 (1933) 342.
- [118] G. Herrmann, *Z. Phys. Chem.* B35 (1937) 298.

- [119] J.P. Blewett, H.A. Liebhafsky, E.F. Hennelly, *J. Chem. Phys.* 7 (1939) 478.
- [120] M.G. Inghram, W.A. Chupka, R.F. Porter, *J. Chem. Phys.* 23 (1955) 2159.
- [121] S.A. Shchukarev, G.A. Semenov, *Zhur. Neorg. Khim.* 2 (1957) 1217.
- [122] R.S. Newbury, G.W. Barton, A.W. Searcy, *J. Chem. Phys.* 48 (1968) 793.
- [123] G.A. Semenov, O.S. Popkov, A.I. Soloveichik, S.N. Persian'ova, *Russ. J. Phys. Chem.* 46 (1972) 898.
- [124] M. Hilpert, H. Gerads, *High Temp. Sci.* 7 (1975) 11.
- [125] Le Chatelier, *Compt. Rend.* 115 (1892) 655.
- [126] J.H. Hildebrand, *J. Am. Chem. Soc.* 34 (1912) 246.
- [127] L. Till, *J. Therm. Anal.* 3 (1971) 177.
- [128] G.A. Emel'chenko, N.V. Abrasimov, A.V. Bazhenov, V.M. Masalov, A.A. Zhokhov, P.A. Kononovich, G.Y. Logvenov, S. Khasarov, *IEEE Trans. Magn.* 27 (1991) 1146.